

METHOD

Open Access



Linking single-cell measurements of mass, growth rate, and gene expression

Robert J. Kimmerling^{1,2}, Sanjay M. Prakadan^{1,3,4,5,6}, Alejandro J. Gupta^{1,3,4,5,6}, Nicholas L. Calistri¹, Mark M. Stevens^{1,7}, Selim Olcum¹, Nathan Cermak¹, Riley S. Drake^{1,3,4,5,6}, Kristine Pelton⁸, Frederik De Smet⁹, Keith L. Ligon⁸, Alex K. Shalek^{1,3,4,5,6,10,11*} and Scott R. Manalis^{1,2,12*}

Abstract

Mass and growth rate are highly integrative measures of cell physiology not discernable via genomic measurements. Here, we introduce a microfluidic platform enabling direct measurement of single-cell mass and growth rate upstream of highly multiplexed single-cell profiling such as single-cell RNA sequencing. We resolve transcriptional signatures associated with single-cell mass and growth rate in L1210 and FL5.12 cell lines and activated CD8+ T cells. Further, we demonstrate a framework using these linked measurements to characterize biophysical heterogeneity in a patient-derived glioblastoma cell line with and without drug treatment. Our results highlight the value of coupled phenotypic metrics in guiding single-cell genomics.

Keywords: Single-cell RNA-Seq, Mass, Growth, Serial suspended microchannel resonator, Multi-omics, Single cell, T cell activation, Glioblastoma, GBM, Drug response, Microfluidics, Biophysical properties

Background

Recent experimental advancements have dramatically improved the throughput and cost-efficiency of single-cell RNA sequencing (scRNA-seq) [1–3]. However, gene expression measurements alone cannot fully describe many complex cellular processes [4, 5]. Thus, parallel efforts have focused on linking single-cell transcriptomics with complementary data that can provide further information to help guide analyses and contextualize distinct cellular states. For instance, various multi-omic methods have been developed to link measurements such as protein abundance, DNA sequence, or methylation with gene expression from the same single cell [6–9]. Gene expression measurements have also been linked to single-cell location within a tissue to enable study of cellular development and differentiation at unprecedented detail [10–12]. Moreover, single-cell functional assays have been coupled with mRNA expression to obtain novel insights into the relationships among cellular electrophysiology, morphology, and transcription [13]. Taken together,

these approaches demonstrate how linked single-cell data sets can afford a deep understanding of various cellular phenotypic states that may be difficult to glean through transcriptomic measurements alone.

Linked gene expression data sets are of particular interest when considering recent technological developments that enable the precise measurement of various single-cell biophysical properties, such as mass and growth rate [14, 15]. As highly integrative metrics of cellular state, these parameters offer unique insights into a wide range of biological phenomena, including (i) basic patterns of single-cell mass and growth regulation; (ii) biophysical changes associated with immune cell activation; and, (iii) cancer cell heterogeneity in the presence or absence of drug [16–18]. However, the approaches and devices previously used to collect these biophysical measurements have precluded linking these properties with molecular profiling of the same cell.

To our knowledge, there have been no methods reported to date that allow for linked measurements of cellular mass, growth rate, and transcriptome-wide gene expression from the same cell. It has therefore been challenging to characterize the underlying transcriptional programs associated with cellular mass and

* Correspondence: shalek@mit.edu; srm@mit.edu

¹Koch Institute for Integrative Cancer Research, Massachusetts Institute of Technology, Cambridge, MA 02139, USA

Full list of author information is available at the end of the article



growth rate variability observed in a range of normal and dysfunctional biological contexts.

Here, we describe and characterize a microfluidic platform that enables the measurement of single-cell mass and growth rate immediately upstream of a range of highly multiplexed single-cell endpoint assays. We leverage this approach in combination with scRNA-seq to examine linked single-cell biophysical and transcriptomic properties in cell lines and primary cells. Finally, we apply this method to examine biophysical heterogeneity in a patient-derived glioblastoma (GBM) cancer cell line in the presence or absence of drug, highlighting the potential utility of guiding single-cell genomic measurements with biophysical metadata.

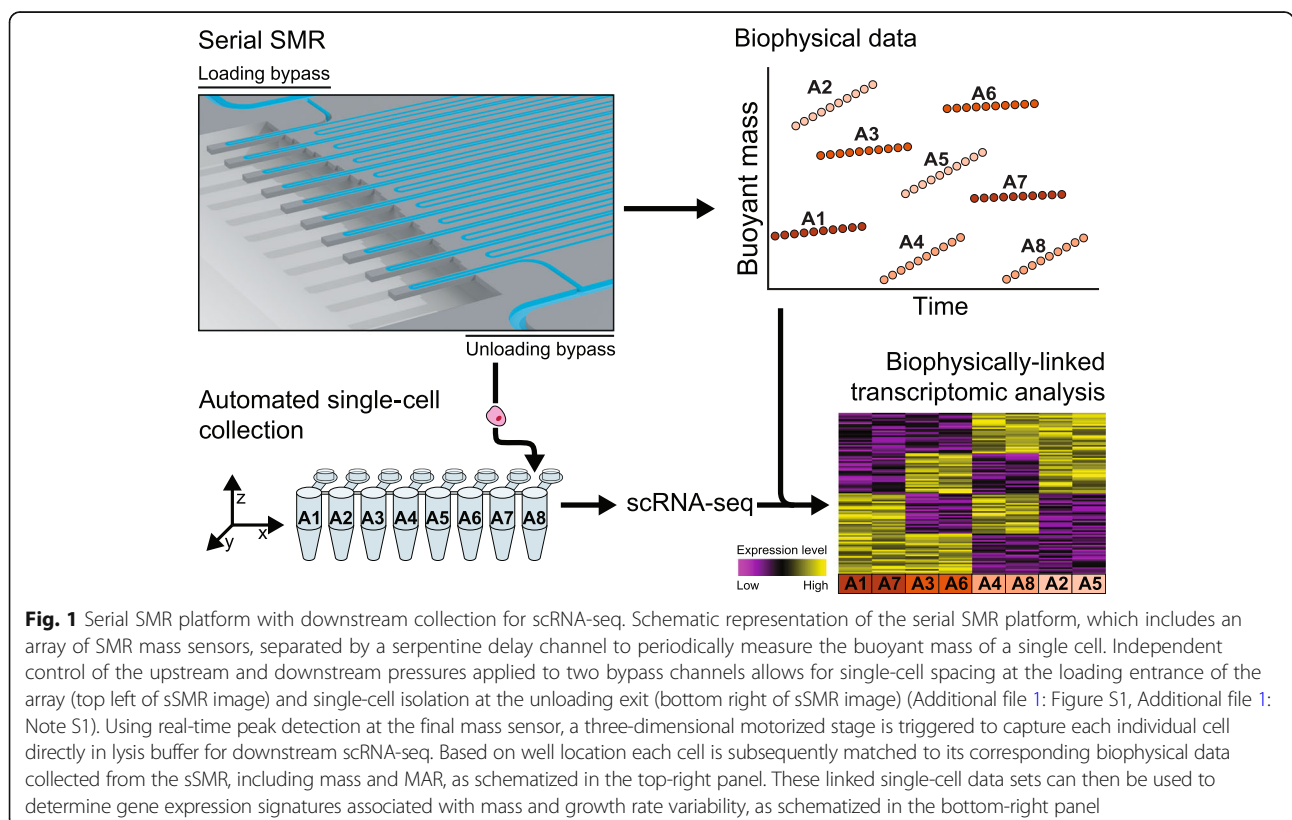
Results and discussion

Serial SMR platform with downstream collection for scRNA-seq

Our system relies on a modified version of a previously described serial suspended microchannel resonator (sSMR) device (Fig. 1) that utilizes an array of high-resolution single-cell buoyant mass sensors placed periodically along the length of a long microfluidic channel to allow a single cell's mass to be measured periodically as it traverses the channel [17]. In addition to providing mass information, this series of measurements can also be used to determine the mass

accumulation rate (MAR), or growth rate, of each cell. Here, taking advantage of real-time access to the data generated by each SMR mass sensor, we have modified the system to use peak detection in the final cantilever. Detection at this cantilever indicates a cell exiting the mass sensor array and triggers the motion of a three-dimensional motorized stage which positions a PCR tube containing lysis buffer to capture each single cell as it is flushed from the system. This enables, for the first time, measurements of the biophysical properties of mass and growth rate to be linked to genomic profiles—here RNA-seq—at the single-cell level (Methods).

We sought to endow our platform with sufficiently high throughput to enable measurements on populations of cells that may change over time. The total time required to flush the system's dead volume and release each single cell (20 s for the system implementation described here) sets a theoretical maximum throughput for the platform to avoid the collection of multiplets. Crucially, to minimize the frequency of failed capture events, we implemented a new fluidic scheme whereby single cells are loaded into the array of mass sensors at fixed intervals (Additional file 1: Figure S1, Additional file 1: Note S1) [19]. Ultimately, this fluidic scheme allows us to achieve a throughput of one cell approximately every 30 s (for a throughput of up to 120 cells per hour) with minimal failed collection



events due to co-release. This offers a two-fold throughput improvement over previous implementations of biophysical measurements alone, while affording the additional ability to capture each individual cell downstream for processing—e.g., scRNA-seq.

Unique gene expression profiles related to specific biophysical properties and underlying cell biology

To validate our method for collecting linked single-cell biophysical and gene expression data, we first measured two murine lymphoblast cell lines (L1210 and FL5.12) that have well-characterized mass and growth properties that are stable over the course of long-term propagation in bulk culture (Fig. 2) [15–17, 20]. Single cells collected downstream of the sSMR for scRNA-seq consistently yielded high-quality cDNA libraries, with 85 out of 87 individual L1210 cells and 124 out of 144 individual FL5.12 cells with paired biophysical data passing initial quality controls (e.g., number of genes detected greater than 4000, [Methods](#), Additional file 1: Figure S2).

In order to determine the transcriptional signatures associated with the spectrum of biophysical states in these cells, we ranked genes by how strongly their expression levels correlated with single-cell biophysical data (Spearman’s correlation coefficients, Additional file 2: Table S1; NB Both Spearman and Pearson correlation methods yielded similar results for all comparisons considered, Additional file 1: Figure S3). We then utilized the GSEA Preranked tool to determine which gene sets showed significant enrichment at either end of these ranked lists (FDR < 0.05, [Methods](#), Additional file 3: Table S2) [21]. For both cell lines, genes ranked by correlation strength with single-cell mass (final mass measurement collected before cell lysis) were highly enriched for functional annotations relating to cell cycle progression (FDR < 0.05, Additional file 3: Table S2, Fig. 2). Specifically, genes related to early cell cycle events immediately following cell division—such as DNA replication initiation—were more highly expressed in cells with lower masses, whereas genes related to late cell cycle events that occur just prior to division—such as chromosome segregation—were

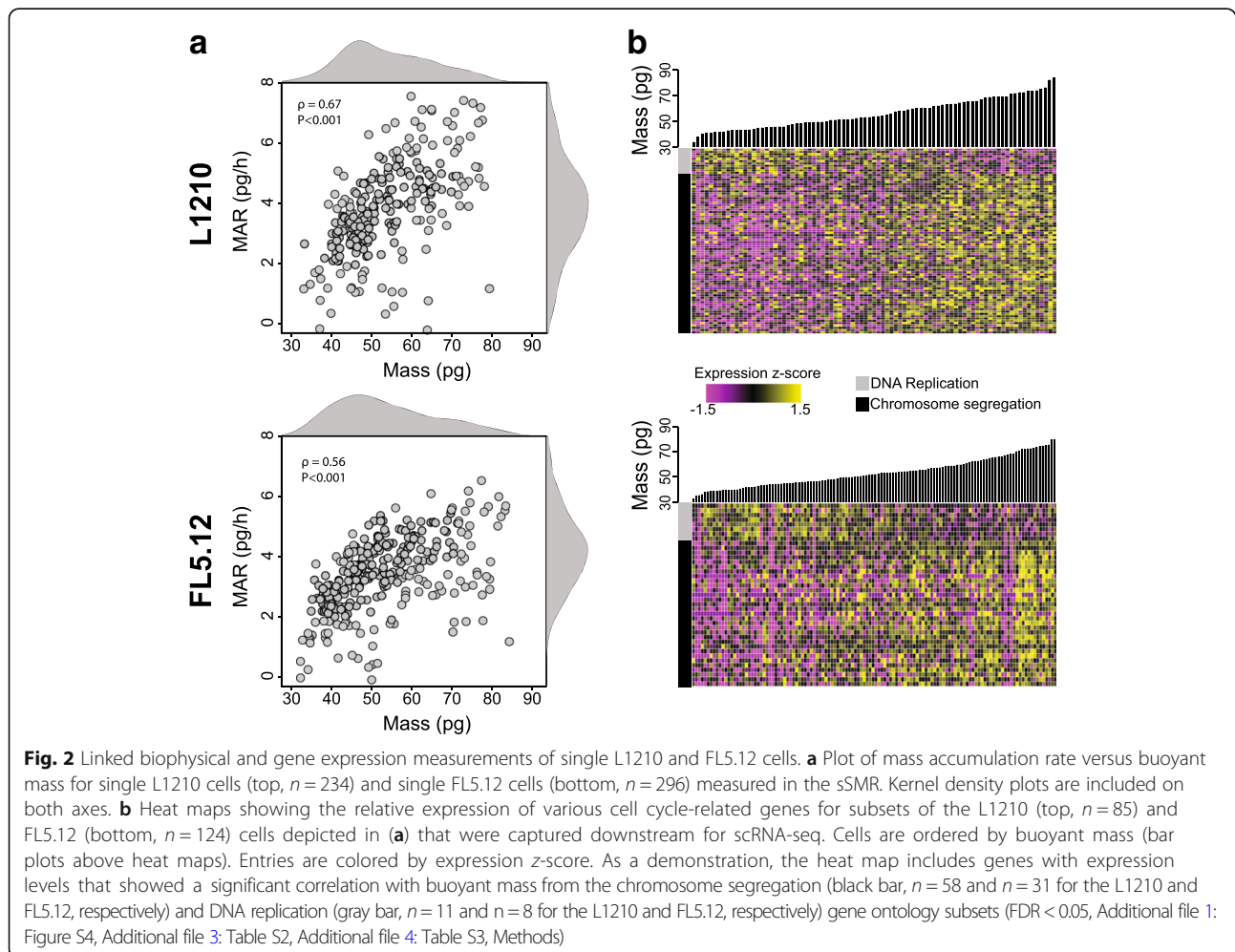


Fig. 2 Linked biophysical and gene expression measurements of single L1210 and FL5.12 cells. **a** Plot of mass accumulation rate versus buoyant mass for single L1210 cells (top, $n = 234$) and single FL5.12 cells (bottom, $n = 296$) measured in the sSMR. Kernel density plots are included on both axes. **b** Heat maps showing the relative expression of various cell cycle-related genes for subsets of the L1210 (top, $n = 85$) and FL5.12 (bottom, $n = 124$) cells depicted in **(a)** that were captured downstream for scRNA-seq. Cells are ordered by buoyant mass (bar plots above heat maps). Entries are colored by expression z-score. As a demonstration, the heat map includes genes with expression levels that showed a significant correlation with buoyant mass from the chromosome segregation (black bar, $n = 58$ and $n = 31$ for the L1210 and FL5.12, respectively) and DNA replication (gray bar, $n = 11$ and $n = 8$ for the L1210 and FL5.12, respectively) gene ontology subsets (FDR < 0.05, Additional file 1: Figure S4, Additional file 3: Table S2, Additional file 4: Table S3, [Methods](#))

more highly expressed in cells with higher masses (Additional file 4: Table S3). Interestingly, both cell lines revealed a larger number of genes that showed a significant positive correlation with mass relative to the number of genes with a significant negative correlation, though this may be impacted, in part, by the transcript capture inefficiencies inherent in scRNA-seq protocols (Additional file 1: Figure S4) [22].

The manifestation of cell cycle-related gene expression in scRNA-seq data has been of particular interest to both further characterize mechanisms of cell cycle progression and regress out the contributions of cell cycle variability that may act as a nuisance parameter, dominating gene expression heterogeneity among single cells and masking more subtle biological signals [2, 23, 24]. We therefore sought to determine how previously annotated cell cycle signatures corresponded to the single-cell mass measurements collected here. To do so, we established cell cycle phase-specific (G1/S and G2/M) scores using an approach inspired by Macosko et al. [2] (Additional file 1: Figure S5, Additional file 1: Note S3). Cells assigned to either the G1/S or G2/M phases of the cell cycle using gene expression data alone showed significant differences in cell mass for both the L1210 and FL5.12 cells that were consistent with expectations (i.e., lower mass for G1/S cells; $P < 0.001$, Mann-Whitney U test). Furthermore, for both cell types, cell mass showed a clear negative correlation with G1/S scoring ($\rho = -0.46$ and $\rho = -0.25$ for L1210 and FL5.12, respectively; $P < 0.005$) and a clear positive correlation with G2/M scoring ($\rho = 0.74$ and $\rho = 0.54$ for L1210 and FL5.12, respectively; $P < 0.001$). Together, these results provide additional evidence of coordination between cell mass and cell cycle-related gene expression in actively proliferating cells.

To further confirm the consistency and reproducibility of the linked biophysical and gene expression data sets collected with this platform, we compared the L1210 and FL5.12 results with scRNA-seq data from additional independent experiments. For L1210 cells, we found that genes that showed significant correlations with cell mass were also significantly enriched among those previously shown to correlate with time since cell division, a proxy for cell cycle progression (FDR < 0.05 , Additional file 1: Figure S6, Additional file 1: Note S2) [25]. In FL5.12 cells, meanwhile, we observed that the genes which showed significant correlations between their expression levels and biophysical properties were highly reproducible across two independent linked biophysical and gene expression experiments (FDR < 0.05 , Additional file 1: Figure S6, Additional file 1: Note S2). These results demonstrate the quality and reproducibility of transcriptional measurements collected downstream of the sSMR.

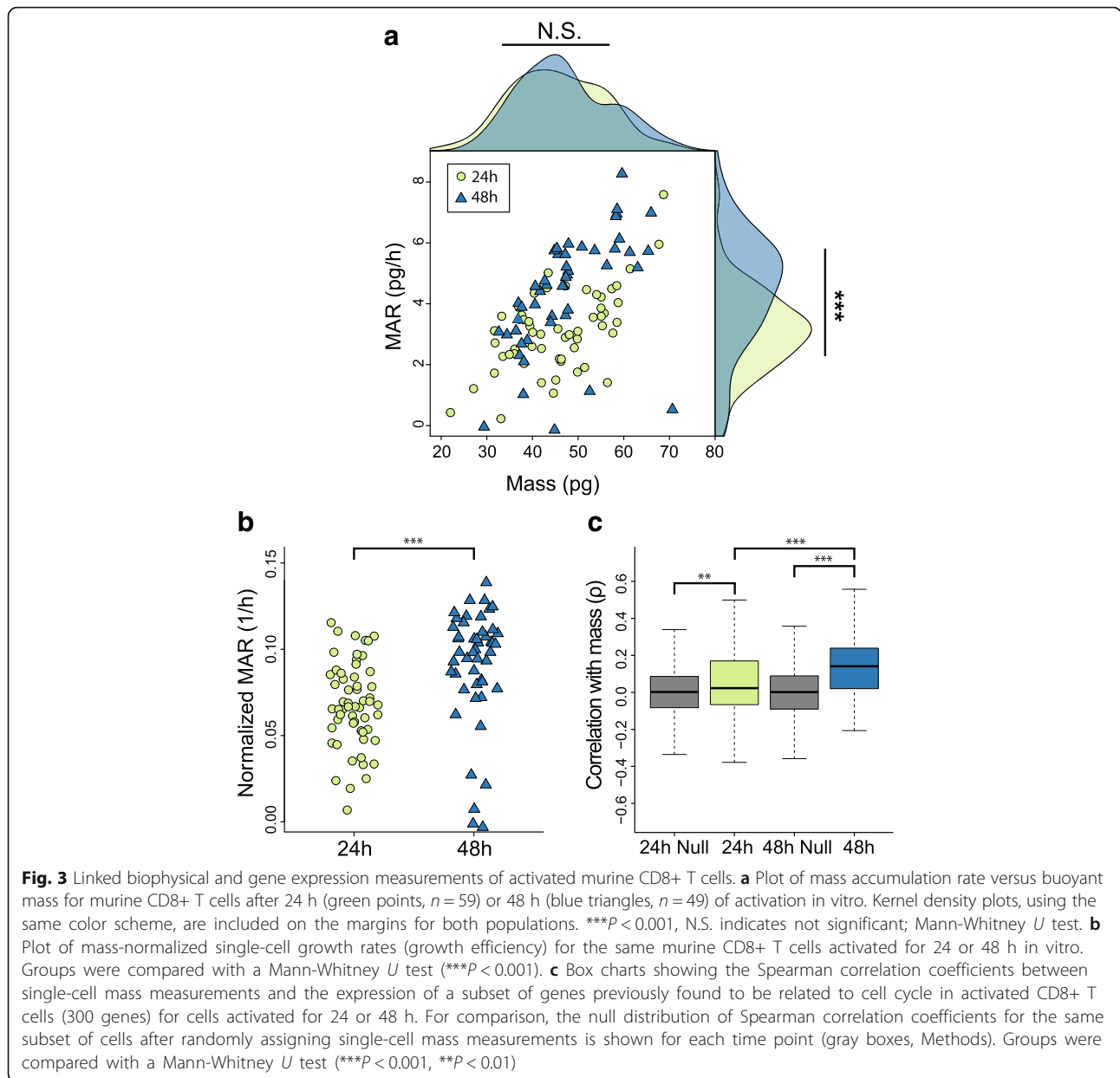
Given that we identified a linear relationship between mass and MAR in these cell types ($\rho = 0.67$ and $\rho = 0.56$ for L1210 and FL5.12, respectively; $P < 0.001$, Fig. 2), we focused our analysis on mass-normalized MAR, determined by dividing each cell's MAR by its corresponding mass. We used this parameter, which measures a single cell's growth efficiency decoupled from mass-related confounders, to resolve growth-related transcriptional signatures in these two cell lines [18, 26]. For L1210 cells, genes ranked by strength of correlation between expression level and growth efficiency did not reveal any statistically significant enrichment of functional annotations (FDR > 0.05). The FL5.12 cells, however, showed significant positive enrichment for functional annotations related to cell cycle progression among genes ranked by correlation strength with growth efficiency (FDR < 0.05 , Additional file 3: Table S2). Specifically, subsets of genes implicated in the G1-S transition showed a higher level of expression in cells of intermediate mass with the highest growth efficiencies (Methods, Additional file 1: Figure S7, Additional file 5: Table S4) [27]. These results are consistent with previous FL5.12 single-cell growth measurements, which revealed an increase in growth efficiency approaching the G1-S transition followed by a decrease later in the cell cycle [15].

Characterizing CD8+ T cell activation with linked biophysical and gene expression measurements

While the L1210 and FL5.12 cells represent effective model systems with stable biophysical and transcriptional profiles, one of the benefits of the sSMR platform is that it offers sufficient throughput to characterize cell populations that may be changing in their phenotypes over time [20, 25]. Primary CD8+ T lymphocytes are a prime example of a cell population that may exhibit dynamic behavior, as they are known to drastically change their biophysical properties, transcriptional states, and metabolic characteristics in response to activation [17, 28, 29].

To characterize this response, we collected single-cell biophysical and gene expression profiles from freshly isolated, naïve murine CD8+ T cells which we stimulated in vitro with antibody-based T cell receptor engagement and CD28 co-stimulation (Fig. 3, Methods). We chose to evaluate the 24 and 48 h time points to capture cells before and after their first division event, respectively [30]. Although the cells for both time points displayed similar mass distributions, the cells measured after 48 h of activation showed significantly higher growth efficiencies ($P < 0.001$, Mann-Whitney U test, Fig. 3a, b).

Examining gene expression alone, we observed that cells from these two populations showed differential



expression patterns consistent with T cell activation, including significant upregulation of Granzyme B (*Gzmb*) and IL-2 receptor (*Il2ra* and *Il2rb*), as well as significant downregulation of *Ccr7* in the 48 h population compared to the 24 h one (Bonferroni-corrected $P < 0.05$, Additional file 6: Table S5). Similarly, gene set enrichment analysis performed on genes ranked by expression fold change between these time points revealed significant enrichment for gene sets related to immune cell effector function and glucose metabolism, consistent with functional and metabolic shifts that have been previously characterized in activated CD8+ T cells (FDR < 0.05 , Additional file 7: Table S6, Additional file 8: Table S7) [28, 31]. Cells activated for

48 h also displayed a higher expression of genes related to protein production, including those involved in translation initiation and cytosolic ribosome activity (Additional file 8: Table S7). Araki et al. recently demonstrated a similar trend, noting an increase in translation activity over the course of early T cell activation, as cells become more proliferative [32]. The measurements presented here suggest that this increase in translation activity is accompanied by, and potentially is tied to, increased growth efficiency observed at 48 h compared to 24 h.

This population-level relationship between growth efficiency and translation-related gene expression was also observable at the single-cell level for cells activated for 48 h. Within this time point, genes ranked by

correlation strength with single-cell growth efficiency once again showed significant enrichment for functional annotations relating to translation machinery (FDR < 0.05, Additional file 3: Table S2). Despite a similar number of genes showing a significant correlation with growth efficiency at the 24 h time point, these genes did not show any significant functional enrichment when ranked by correlation strength (FDR > 0.05, Additional file 1: Figure S4). This result suggests that the coordination between single-cell growth efficiency and translation-related gene expression occurs later during T cell activation.

The 48 h time point also revealed a greater number of genes that showed a significant correlation between expression level and cell mass relative to the 24 h time point (Additional file 1: Figure S4). When determining the functional role of genes ranked by expression correlation with single-cell mass, the 48 h time point demonstrated significant cell cycle functional enrichment (FDR < 0.05) whereas the 24 h time point only showed a slight enrichment for similar cell cycle-related annotations (FDR < 0.1) and no significantly enriched terms otherwise (Additional file 3: Table S2). However, when conducting a cell cycle phase scoring analysis similar to that described for the L1210 and FL5.12 cells, we found that both the 24 and 48 h time points showed a significant difference in mass between cells assigned to the G1/S and G2/M phases of the cell cycle ($P < 0.001$, Mann-Whitney U test, Additional file 1: Figure S5). Furthermore, a previously described set of genes known to correlate with an activated CD8⁺ T cell's time since division—a proxy for cell cycle progression—showed a significant positive correlation with cell mass in both the 24 h and 48 h populations, though the strength of this correlation did increase significantly by 48 h ($P < 0.001$, Mann-Whitney U test, Fig. 3) [25]. As mentioned above, the 24 and 48 h time points capture cells before and after their first division event, respectively [30]. Although cells are accumulating mass, or “blasting,” in the first 24 h, it is not until roughly 30 h that cells undergo their first division and begin increasing in number and cycling in the traditional sense [30, 33]. Taken together, these results suggest that the coordination between cell cycle gene expression and cell mass begins early during T cell activation, even before cells begin proliferating, and increases in strength later in T cell activation as cells begin actively dividing.

Characterizing single-cell biophysical heterogeneity of a patient-derived cancer cell line

Cancer cell drug responses are known to be highly heterogeneous at the single-cell level [18, 26], and it is now well established that the presence of even a small fraction of cells that are unresponsive to therapy can

lead to resistance and recurrence of cancers [34]. Single-cell transcriptional profiling has been shown to provide a powerful means of characterizing such heterogeneity in clinically relevant tissue samples [35, 36], yet the direct interrogation of drug response is still most commonly measured in clinical trials and the laboratory using bulk viability assays [37]. Although effective in quantifying the relative fraction of resistant cells within a heterogeneous population, these assays rely on endpoint measurements. Taken too late, they may miss responding cells (which are lost to cell death) and/or the preceding molecular events that impact survival; taken too early, bulk measurements can muddle the features of responding and non-responding cell subsets (Fig. 4a). However, we have previously shown that, prior to viability loss, single-cell biophysical changes of mass and MAR collected with the SMR can predict response to drug treatment [18]. Therefore, we reasoned that downstream molecular characterization could be used to further contextualize single-cell mass and growth rate heterogeneity both at baseline and in response to perturbation with drug treatment.

To demonstrate a framework for the characterization of single-cell biophysical heterogeneity in the presence or absence of drug, we decided to measure the effect of an MDM2 inhibitor (RG7388, Roche) on BT159 cells, a patient-derived cell line (PDCL) generated from a primary glioblastoma (GBM) (Methods). GBM PDCLs are known to be particularly heterogeneous with respect to cell lineage and have a cancer stem cell like hierarchy proposed to contribute to profound treatment resistance of these tumors [38]. MDM2, meanwhile, typically binds to p53 inhibiting its transcriptional activity and leading to proteasome-mediated degradation [39]. In prior work, we showed pharmacologic inhibition of MDM2 was a promising therapeutic avenue in GBM patients with wild-type TP53 because in preclinical patient derived models, the drug leads to increased expression and stability of p53, significant responses and even tumor regression via induction of apoptotic cell death [40]. However, in vivo testing revealed that, upon withdrawal of MDM2 inhibition, tumors consistently relapsed, suggesting variable response to treatment [40].

To characterize biophysical heterogeneity at the single-cell level, we collected linked mass, MAR and gene expression measurements for single BT159 cells that had either been treated for 16 h with RG7388 or DMSO (control) (Methods). Overall, the drug-treated population of cells showed a marked reduction in average MAR and an increase in average mass as compared to the control population of cells, as expected from cell cycle exit and apoptosis ($P < 0.001$, Mann-Whitney U test, Fig. 4b). However, there was also considerable heterogeneity in biophysical response to drug, with

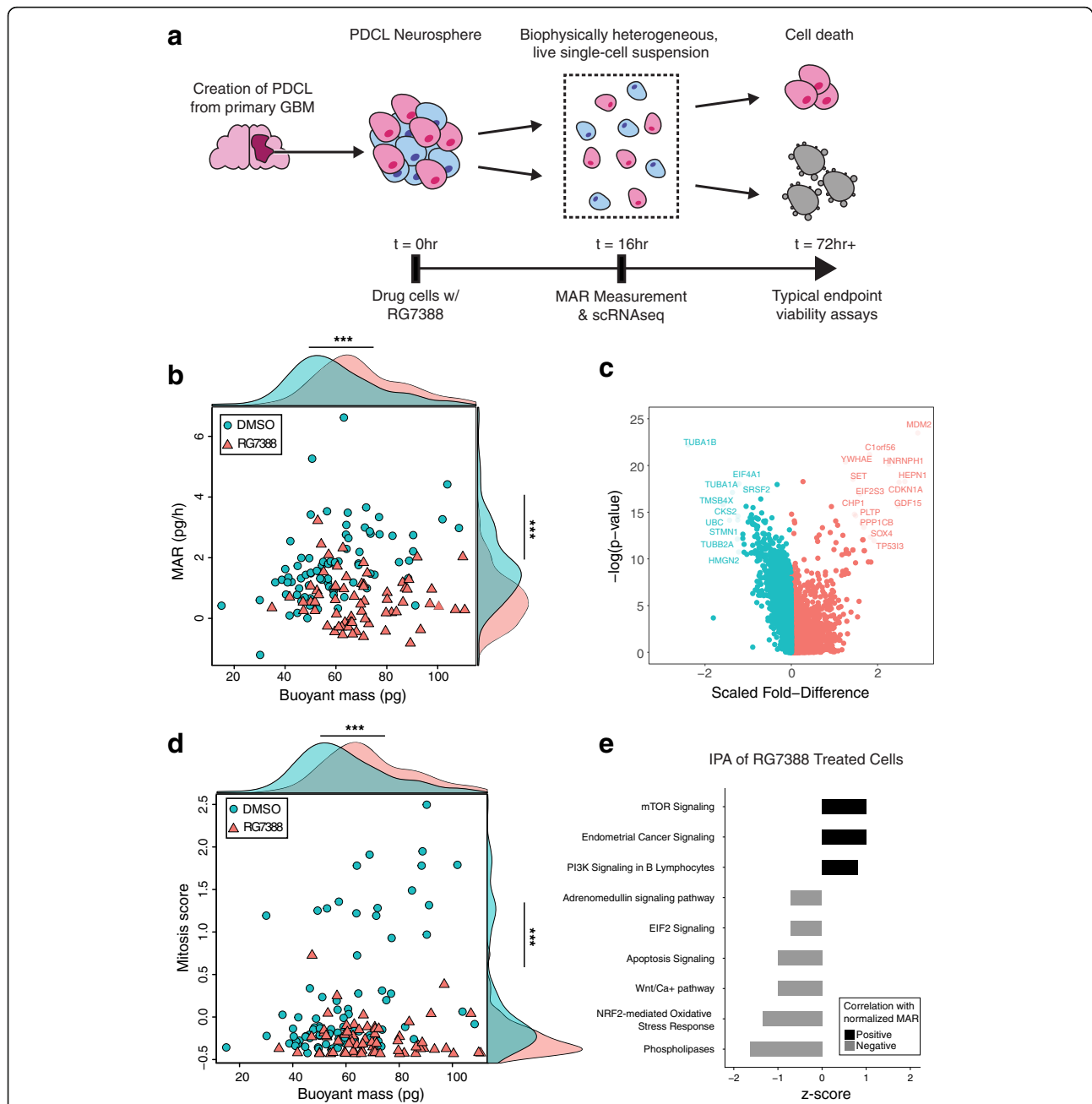


Fig. 4 Characterizing single-cell drug response in BT159 GBM cells. **a** Schematic representation of GBM PDCL generation, drug treatment in vitro, and subsequent characterization of therapeutic response using the sSMR collection platform. Mass and growth measurements are collected after 16 h of treatment, prior to loss of cell viability, which enables downstream molecular characterization with scRNA-seq (Methods). **b** Plot of single-cell MAR versus mass for BT159 GBM cells treated with either DMSO (blue circles, $n = 83$) or RG7388 (an MDM2 inhibitor, red triangles, $n = 66$) for 16 h. Kernel density plots, using the same color scheme, are included in the margins for both populations. $***P < 0.001$, Mann-Whitney U test. **c** Volcano plot showing log-transformed average expression fold change and log-transformed P -values (Bonferroni corrected) for genes upregulated (red) or downregulated (blue) in BT159 cells treated with RG7388 as compared with DMSO treatment. **d** Plot of mitosis scores versus buoyant mass for BT159 cells treated with DMSO (blue circles, $n = 83$) or RG7388 (red triangles, $n = 66$) for 16 h. Mitosis scores were calculated by taking the average z-score adjusted gene expression values of a panel of mitosis-related genes ($n = 29$, Additional file 10: Table S9; Methods). Kernel density plots, using the same color scheme, are included in the margins for both populations. $***P < 0.001$, Mann-Whitney U test. **e** Plot of significantly enriched canonical pathways (FDR < 0.05) in RG7388-treated BT159 cells ($n = 66$), as determined by ingenuity pathway analysis, among genes with significant positive (black) or negative (gray) correlations with normalized MAR. (Additional file 1: Figure S4, Additional file 11: Table S10, Methods)

some cells continuing to show a positive MAR at the time of measurement (Additional file 1: Figure S8). Since these measurements were collected at a single time point, it is difficult to assess whether the cells that continue to grow in the presence of drug are, in fact, resistant to therapy or simply display a delayed response to treatment. Nonetheless, the biophysical heterogeneity found in these results affords the opportunity to determine transcriptional signatures that correlate with this variability at this particular time point.

We next considered only the transcriptional data. As expected, an unbiased analysis (dimensionality reduction by principal components analysis (PCA) and visualization using a t-stochastic neighbor-embedding (tSNE) plot, Methods) revealed distinct transcriptional profiles for drug-treated and control cell populations (Additional file 1: Figure S9a). Relative to DMSO-treated cells, drug-treated cells displayed gene expression signatures consistent with the mechanism of MDM2 inhibition, with genes positively regulated by p53, such as *CDK1NA* (p21) and *MDM2*, showing significant upregulation, and genes negatively regulated by p53, such as *CDK1* and *CDC20*, showing significant downregulation (Bonferroni-corrected $P < 0.05$, Fig. 4c, Additional file 9: Table S8) [41]. We then performed dimensionality reduction (PCA) and graph-based clustering (k -nearest neighbors, KNN) on the transcriptional data from the drug-treated cells alone and visualized our results using a tSNE plot (Additional file 1: Figure S9b; Methods). This clustering analysis did not reveal any clear subsets of drug-treated cells with distinctly different responses to MDM2 inhibition.

Since our transcriptional measurements suggested that all MDM2-inhibitor treated cells were actively experiencing drug but our biophysical measurements revealed mass and MAR heterogeneity, we decided to explicitly examine whether the linked nature of our measurements could be used to shed light on the drivers of biophysical variability at this time point after treatment with DMSO or RG7388. When examining linked measurements of gene expression and cell mass in DMSO treated cells, we found that genes ranked by correlation strength with mass were highly enriched for functional annotations relating to cell cycle progression (Additional file 2: Tables S1, Additional file 3: Table S2). Also, as with the other cell types presented here, larger cells in the control population expressed a higher level of genes associated with late cell cycle events, specifically mitosis (Fig. 4d, Additional file 10: Table S9). Interestingly, an unsupervised clustering analysis (PCA followed by KNN clustering, Methods) of the DMSO-treated cells alone revealed two distinct subsets which had significantly different average masses ($P < 0.01$, Mann-Whitney U test, Additional file 1:

Figure S9c,d), and an upregulation of genes relating to cell cycle progression in the subset with a larger average mass (Additional file 1: Figure S9e).

MDM2 inhibitor-treated cells, meanwhile, showed significantly reduced expression of mitosis-specific genes ($P < 0.001$, Mann-Whitney U test, Fig. 4d). Moreover, in these cells, we did not observe any significant cell cycle-related functional enrichments among those genes correlated with cell mass (FDR > 0.05). These results demonstrate that upon MDM2 inhibition and stabilization of p53 signaling in these cells, cell cycle arrest is achieved as expected but there is no longer a correlation between cell mass and cell cycle-related gene expression ($\rho = 0.47$, $P < 0.001$ for DMSO-treated cells; $\rho = -0.07$, $P = 0.54$ for drug-treated cells). Furthermore, since a subset of cells within the drug-treated population displayed a positive MAR despite ablated cell cycle gene expression (Fig. 4b), our data suggest that cell cycle gene expression alone does not fully account for variability in the single-cell biophysical response. In fact, we did not observe a significant correlation between PCs computed for the drug-treated single-cell transcriptomes and any biophysical properties measured ($P > 0.05$; Methods).

To determine transcriptional signatures that may underlie this biophysical heterogeneity, we utilized the corresponding single-cell MAR data to further contextualize gene expression. Genes ranked by correlation strength with mass-normalized MAR in the MDM2 inhibitor-treated population of cells showed a significant negative enrichment (i.e., higher expression in cells accumulating less mass over time) for functional annotations related to apoptosis regulation, specifically related to p53 signaling (FDR < 0.05 , Additional file 2: Table S1, Additional file 3: Table S2). The DMSO-treated population of cells, meanwhile, did not show any significant functional enrichments among genes ranked by correlation with normalized-MAR (FDR > 0.05 , Additional file 2: Table S1, Additional file 3: Table S2). Similarly, ingenuity pathway analysis (IPA, Qiagen) performed on drug-treated cells revealed significant enrichment of canonical apoptosis signaling among genes showing significant negative correlations with normalized MAR (FDR < 0.05 , Fig. 4e) while the same analysis on DMSO-treated cells did not reveal any apoptosis-related signaling significantly correlated with MAR (FDR > 0.05 , Additional file 1: Figure S10, Additional file 11: S10). Together, these results suggest that cells with a higher normalized MAR had a lower expression of genes related to apoptotic signaling orchestrated by p53, but only in drug treated cells, consistent with the mechanisms of MDM2. IPA of drug-treated cells further revealed partial enrichment (FDR = 0.09) for PTEN signaling (a negative regulator of AKT) and significant enrichment (FDR < 0.05) for mTOR signaling (a positive regulator of AKT)

among genes significantly negatively and positively correlated with normalized MAR, respectively [42, 43]. IPA of DMSO treated cells, however, did not reveal significant enrichment for mTOR or PTEN signaling (FDR > 0.1) in genes correlated with normalized MAR (Additional file 1: Figure S10, Additional file 11: Table S10). Together, these results suggest that cells which continue to grow in the presence of MDM2 inhibition may exhibit more stable AKT signaling, which itself drives MDM2 expression, as compared with cells with decreased normalized MAR, pointing to a potential mechanism of cell survival in the presence of treatment [44, 45]. Though preliminary, these results demonstrate the unique insights offered by linked measurements of biophysical phenotype and gene expression when examining cancer cell drug response at the single-cell level.

Conclusion

The platform presented here enables linked measurements of single-cell biophysical properties and gene expression. Having demonstrated the resolution and reproducibility of these linked data sets with measurements of stable cell lines (L1210 and FL5.12 cells), we present frameworks for two key applications of these linked data sets (i) characterizing immune cell activation and differentiation and (ii) examining cancer cell drug response at the single-cell level.

While the primary focus of this work was on conducting scRNA-seq downstream of the sSMR, we also envision this platform being a useful tool for linking biophysical data with other recently developed approaches that enable DNA sequencing, epigenomic characterization, or multi-omic measurements of single cells [6, 7, 46].

We believe that these linked measurements will offer a novel means of exploring a range of biological questions. For instance, when paired with recently developed computational approaches, these linked biophysical and transcriptional measurements may offer insights into cell cycle regulation as well as provide an additional approach for addressing the potentially confounding effects of cell cycle in scRNA-seq analyses [23]. Clinically, mass and MAR have proven to be effective biomarkers for characterizing cancer cell drug susceptibility at the single-cell level [18, 26]. The ability to link these biophysical measurements with gene expression or genetic profiling offers the exciting opportunity to move beyond the simple classification of responding and non-responding cells and to begin to explore the molecular mechanisms that may drive such behaviors. We envision that this and related approaches may one day inform more effective precision medicine pipelines [47].

Methods

Cell culture and primary cell preparation

L1210 murine lymphocytic leukemia cells (ECACC) were cultured in RPMI 1640 (Gibco) with 10% fetal bovine serum and 1% antibiotic-antimycotic (Gibco). FL5.12 murine pre-B cells (gift from the Vander Heiden Lab, MIT) were cultured in the same media with the addition of 10 ng/ml IL-3 (R&D Systems). For all growth and collection experiments, cells were passaged to a concentration of 5×10^5 cells/ml the night before to ensure consistent culture confluence at time of measurement.

Naïve CD8⁺ T cells were isolated from a 13 week old, male, C57BL/6 J mouse. Splenocytes were subject to red blood cell lysis with ACK buffer (Gibco) followed by naïve CD8⁺ T cell isolation using a MACS-based isolation kit (Miltenyi Biotec). Purified cells were cultured in RPMI 1640 (Gibco) with 10% fetal bovine serum, 55 μ M 2-mercaptoethanol (Gibco), 1% antibiotic-antimycotic (Gibco) and 100 U/ml IL2 (Peprotech). The naïve CD8⁺ T cells were activated in vitro with 5 μ g/ml plate-bound anti-mouse CD3 (clone: 145-2c11, BioLegend), 0.5 μ g/ml plate-bound ICAM-1/CD54 (R&D Systems), and 2 μ g/ml soluble anti-mouse CD28 (clone: 37.51, BioLegend). Cells were seeded at a concentration of 1×10^6 cells/ml in a 96 well plate and activated for either 24 or 48 h prior to measurement in the sSMR.

Primary GBM cells used to generate the BT159 line were harvested from excess tissue resection specimens through cycles of enzymatic (neural tissue dissociation kit with papain, Miltenyi Biotec) and mechanical dissociation in a tissue grinder (gentleMACS dissociator, Miltenyi Biotec). Cells were grown as tumorspheres in NeuroCult NS-A proliferation media (Miltenyi Biotec) supplemented with 2 μ g/ml Heparin, 20 ng/ml human epidermal growth factor (EGF), 10 ng/ml human bFGF in ultra-low attachment coated flasks (Corning). Prior to measurement, the BT159 cells were dissociated with Accutase (Sigma-Aldrich) at 37 °C for 7 min. For drug experiments, cells were treated with 250 nM of the MDM2 inhibitor RG7388 (Roche) or DMSO for 16 h prior to dissociation for measurement.

Single-cell growth measurements and collection

For all experiments, cells were adjusted to a final concentration of 2.5×10^5 cells/ml to load single cells into the mass sensor array as described in Additional file 1: Note S1. Single-cell growth measurements were conducted as described previously [17]. In order to exchange buffer and flush individual cells from the system, the release side of the device was constantly flushed with PBS at a rate of 15 μ L per minute (Additional file 1: Figure S1, P2 to P4). Upon detection of a single-cell at the final cantilever of the sSMR, as indicated by a supra-threshold shift in resonant frequency, a set of three-dimensional motorized stages

(ThorLabs) was triggered to move a custom PCR-tube strip mount from a waste collection position to a sample collection position. The location of these motors was written to a file for the duration of the experiment in order to annotate single-cell mass and MAR measurements with well position, and thus transcriptional profiles, downstream. Each cell was collected in 5 μ l of PBS directly into a PCR tube containing 5 μ l of 2 \times TCL lysis buffer (Qiagen) with 2% *v/v* 2-mercaptoethanol (Sigma) for a total final reaction volume of 10 μ l. After each 8-tube PCR strip was filled with cells, the strip was spun down at 1000 g for 30 s and placed immediately on dry ice. Following collection, samples were stored at -80°C prior to library preparation and sequencing.

scRNA-seq

Single-cell RNA isolation, cDNA library synthesis, next generation sequencing, read alignment and gene expression estimation were performed as described previously [48]. Briefly, Smart-Seq2 whole transcriptome amplification and library preparation were performed on single-cell lysates collected with the sSMR [49]. Single-cell libraries were then sequenced on an Illumina NextSeq 500 using 30-bp paired end reads. Data was initially filtered to exclude cell doublets or cells with failed matching of masses for growth rate measurement. This step left 87 out of 96 total L1210 cells, 144 out of 192 total FL5.12 cells, 178 out of 192 total CD8⁺ T cells, and 181 out of 192 total BT159 GBM cells. Next, cells that exceeded a preliminary complexity threshold (4000 genes for L1210 and FL5.12 cells, 2000 genes for CD8⁺ T cells, or 1000 genes for BT159 cells) were selected for further analysis. Overall, this yielded 85 out of 87 total L1210 cells, 124 out of 144 total FL5.12 cells, 108 out of 178 total CD8⁺ T cells, and 149 out of 192 total BT159 cells. These cells selected for analysis were sequenced to an average depth of $1,698,879 \pm 106,027$ (s.e.m.) reads for L1210 cells, $760,919 \pm 36,679$ (s.e.m.) reads for FL5.12 cells, $1,333,686 \pm 90,744$ (s.e.m.) reads for CD8⁺ T cells, and $993,629 \pm 75,796$ (s.e.m.) reads for BT159 cells respectively. Reads were aligned using TopHat2 and expression estimates (transcripts per million; TPM) for all UCSC-annotated mouse genes (mm10, for L1210, FL5.12, and CD8⁺ T cells) or human genes (hg19, for BT159 cells) were calculated using RNA-seq by expectation maximization (RSEM) [50, 51]. The average transcriptome alignments were $67.4 \pm 0.38\%$ (s.e.m.) for L1210 cells, $64.8 \pm 0.51\%$ (s.e.m.) for FL5.12 cells, $57.3 \pm 1.36\%$ (s.e.m.) for CD8⁺ T cells, and $35.2 \pm 0.84\%$ (s.e.m.) for BT159 cells. The average number of genes detected was $7,207 \pm 94$ (s.e.m.) for L1210 cells, $6,891 \pm 81$ (s.e.m.) for FL5.12 cells,

$5,149 \pm 159$ (s.e.m.) for CD8⁺ T cells, and $5,347 \pm 173$ (s.e.m.) for BT159 cells (Additional file 1: Figure S2).

Gene expression analysis

All analysis was performed on log-transformed expression level measurements ($\ln(\text{TPM} + 1)$). Data pre-processing was conducted with the Seurat package for R [10]. All genes that were detected in $>5\%$ of cells were included in the final analysis for each group of cells (L1210, FL5.12, CD8⁺ T cells, and BT159 GBM cells).

Significance-testing

To define the null distribution of correlation coefficients described in Fig. 3, we determined the Spearman correlation between cell cycle gene expression levels and mass for randomly shuffled data sampled from the experimental values (i.e., mismatching single-cell mass and gene expression data). After 10,000 iterations, we used the average mean and standard deviation values of these correlation coefficient distributions to define the null distributions presented.

We computed the null distributions for the correlation coefficients between either mass, MAR, or normalized MAR and the principal components for either the DMSO-treated, drug-treated, or combined transcriptomic data sets using a similar random shuffling of PC coordinates across single-cells. Following 10,000 iterations, the mean and standard deviation of these distributions were compared to the correlation of each biophysical parameter with all significant principal components (PCs). For each data set, the PCElbow plot and jackstraw functions in Seurat were used to select significant PCs whose explained variation preceded a precipitous drop in cumulative explained variation (elbow). In each data set, for consistency, the top 10 PCs were investigated, although in some cases fewer than 10 PCs preceded the elbow. Correlation coefficients were deemed insignificant if they were within two standard deviations of the mean determined from random shuffling.

Gene set enrichment analysis

Ranked gene lists were created for each cell population by determining the gene-wise correlation coefficient (Spearman) between log-transformed gene expression levels and either single-cell mass or growth efficiency (MAR/mass; Additional file 2: Table S1). Spearman and Pearson correlation coefficients yielded similar results for all conditions measured (Additional file 1: Figure S4). Gene set enrichment was computed for these ranked lists using the GSEA Preranked tool, implemented with the fgsea package in R (Additional file 3: Table S2) [21, 52].

Differential expression

Differential expression analysis for the 24 versus 48 h CD8+ T cell measurements, as well as the DMSO versus RG7388 treated BT159 cells, was performed using the FindMarkers function of Seurat with the Wilcoxon rank sum test (Additional file 6: Table S5, Additional file 9: Table S8). For the CD8+ T cells, genes were also ranked by log-normalized fold-change expression difference between the 24 and 48 h time points and analyzed with the GSEA Preranked tool (Additional file 7: Table S6, Additional file 6: Table S5). All *P* values presented are Bonferroni corrected, as per Seurat documentation recommendation.

Dimensionality reduction

Variable genes for the DMSO-treated, drug-treated, and combined data sets were identified using Seurat's FindVariableGenes. Principal components analysis (PCA) was performed over these genes for each of the three sets of cells, followed by non-linear dimensionality reduction by t-stochastic neighbor embedding (tSNE). Clusters were identified in the linear PC space using *K*-nearest neighbor (KNN) clustering, and cluster assignments were visualized on the non-linear tSNE space. For the DMSO-treated cells, we detected two distinct clusters (Additional file 1: Figure S9c); for the RG7388 treated cells, we only detected one (Additional file 1: Figure S9b).

Ingenuity pathway analysis

Ingenuity pathway analysis (IPA, Qiagen) was performed on canonical pathways using genes which significantly correlated positively and negatively with normalized MAR (Additional file 1: Figure S4). Briefly, correlation and *P* values for significant genes were uploaded into IPA and analyzed using the "Core Analysis" function. Correlations were input as "Expression: Other" measurements with range from $-\infty$ to ∞ . Significant canonical pathways and upstream regulators (determined by hypergeometric test) with positive and negative *z*-scores are plotted in Fig. 4e.

Additional files

Additional file 1: Supplementary figures and notes. (PDF 14878 kb)

Additional file 2: Table S1. Gene lists ranked by correlation with either mass or mass-normalized MAR for L1210, FL5.12, CD8+ T cells (24 and 48 h activations), and BT159 GBM cells (DMSO and RG7388 treated) with corresponding Spearman correlation coefficients. Genes that are either significantly positively or negatively correlated with the biophysical measurement of interest (as described in Additional file 1: Figure S4) are highlighted in red. (XLSX 3597 kb)

Additional file 3: Table S2. Gene set enrichment reports for all the ranked gene lists presented in Additional file 2: Table S1. Enrichments were generated using the fgsea tool in R. Only gene sets with a false discovery rate (FDR) value less than 0.1 are included. (XLSX 88 kb)

Additional file 4: Table S3. Cell cycle genes significantly correlated with cell mass for L1210 and FL5.12. Genes from the "chromosome segregation" gene ontology term that had a significant positive correlation with cell mass ($n = 58$ and 31 genes for L1210 and FL5.12 cells, respectively) and genes from the "DNA replication" gene ontology term with a significant negative correlation with cell mass ($n = 11$ and 8 genes for L1210 and FL5.12 cells, respectively) were used to construct the lists for each cell type. Significance was determined as described in Additional file 1: Figure S4. (XLSX 9 kb)

Additional file 5: Table S4. List of G1S related genes correlating with normalized growth rate in FL5.12 cells. Genes from the "cell cycle G1 S phase transition" gene ontology term that showed a significant positive correlation with normalized growth rate in FL5.12 cells ($n = 13$ genes, as described in Additional file 1: Figure S7) were used to construct this gene list. (XLSX 8 kb)

Additional file 6: Table S5. List of significantly differentially expressed genes between the 24 and 48 h time points for the activated CD8+ T cells with corresponding Bonferroni-corrected *P* values and log-normalized fold change values. Negative values indicate genes expressed at a higher level in the 48 h time point. (XLSX 24 kb)

Additional file 7: Table S6. CD8+ T cell gene list ranked by log-normalized fold change in gene expression between the 24 and 48 h activation time points. Negative values indicate genes expressed at a higher level in the 48 h time point. (XLSX 43 kb)

Additional file 8: Table S7. Gene set enrichment report for the ranked gene list presented in Additional file 7: Table S6. Enrichments were generated using the fgsea tool in R. Only gene sets with a false discovery rate (FDR) value less than 0.1 are included. (XLSX 17 kb)

Additional file 9: Table S8. List of significantly differentially expressed genes between the DMSO and RG7388 treated BT159 GBM cells with corresponding Bonferroni-corrected *P* values and log-normalized fold change values. Negative values indicate genes that were expressed at a higher level in the DMSO treated cells. (XLSX 451 kb)

Additional file 10: Table S9. List of mitosis related genes correlating with mass in DMSO treated BT159 GBM cells. Genes from the "mitosis" gene ontology term that showed a significant positive correlation with cell mass in the DMSO treated BT159 GBM cells ($n = 29$ genes, as described in Additional file 1: Figure S4) were used to construct this gene list. (XLSX 8 kb)

Additional file 11: Table S10. Table of ingenuity pathway analysis (IPA) results for canonical pathway analysis of genes significantly positively or negatively correlated with normalized MAR in RG7388 or DMSO treated BT159 cells (Additional file 1: Figure S4, Fig. 4, Additional file 1: Figure S10, Methods). The table includes all pathways with an FDR < 0.1. (XLSX 20 kb)

Abbreviations

FDR: False discovery rate; MAR: Mass accumulation rate; scRNA-seq: Single-cell RNA sequencing; sSMR: Serial suspended microchannel resonator

Funding

This work was supported by Cancer Systems Biology Consortium U54 CA217377 (S.R.M. and A.K.S.), R33 CA191143 (S.R.M.), R01 CA170592 (S.R.M., K.L.L.), the Searle Scholars Program (A.K.S.), the Beckman Young Investigator Program (A.K.S.), NIH New Innovator Award 1DP2GM119419 (A.K.S.), NIH 5U24AI118672 (A.K.S.), NIH 1R33CA202820 (A.K.S.), NIH 2U19AI089992 (A.K.S.), NIH 1R01HL134539 (A.K.S.), NIH 2RM1HG006193 (A.K.S.), 2P01AI039671 (A.K.S.), the Pew-Stewart Scholars (A.K.S.), a Sloan Fellowship in Chemistry (A.K.S.), and partially by Cancer Center Support (core) Grant P30-CA14051 from the National Cancer Institute (S.R.M. and A.K.S.).

Availability of data and materials

All RNA-seq data generated in this study has been deposited into the Gene Expression Omnibus database hosted at the National Center for Biotechnology Information under the accession code GSE121655 [53]. All R code used for data analysis has been deposited in a public GitHub repository (<https://github.com/rjkimmer/linkedMeasurementAnalysis>) [54].

Authors' contributions

RJK, NLC, SO, NC, and SRM designed and implemented the platform. RJK, MMS, FDS, KLL, AKS, and SRM designed the experiments. RJK, AJG, and NLC performed the sSMR experiments. SMP, AJG, and RD performed scRNA-seq. KLL, FDS, and KP performed BT159 cell line development. RJK, SMP, AJG, and MMS analyzed the data. RJK, AKS, and SRM wrote the manuscript, with input from all authors. All authors read and approved the final manuscript.

Ethics approval and consent to participate

The GBM PDCL BT159 was generated using patient tissue collected under a protocol (Dana Farber Harvard Cancer Center protocol #10-043) approved by Dana Farber Harvard Cancer Center and Partner's Human Research Center institutional review boards. All experiments comply with the Declaration of Helsinki. Animals were cared for in accordance with federal, state and local guidelines following a protocol approved by the Department of Comparative Medicine at MIT (protocol number 0317-022-20).

Consent for publication

Not applicable.

Competing interests

RJK, MMS, SO, KLL, and SRM declare competing financial interests as cofounders of Travera, which develops technology relevant to the research presented. SRM declares competing financial interests as a cofounder of Affinity Biosensors, which develops technology relevant to the research presented. KLL declares competing financial interests as a consultant for Bristol-Myers Squibb in a capacity relevant to the research presented.

Publisher's Note

Springer Nature remains neutral with regard to jurisdictional claims in published maps and institutional affiliations.

Author details

¹Koch Institute for Integrative Cancer Research, Massachusetts Institute of Technology, Cambridge, MA 02139, USA. ²Department of Biological Engineering, Massachusetts Institute of Technology, Cambridge, MA 02139, USA. ³Ragon Institute of Massachusetts General Hospital, Massachusetts Institute of Technology, and Harvard, Cambridge, MA 02139, USA. ⁴Department of Chemistry, Massachusetts Institute of Technology, Cambridge, MA 02139, USA. ⁵Institute for Medical Engineering & Science, Massachusetts Institute of Technology, Cambridge, MA 02139, USA. ⁶Broad Institute of MIT and Harvard, Cambridge, MA 02142, USA. ⁷Department of Medical Oncology, Dana-Farber Cancer Institute, Harvard Medical School, Boston, MA 02215, USA. ⁸Department of Oncologic Pathology, Dana-Farber Cancer Institute, Boston, MA 02215, USA. ⁹Department of Imaging and Pathology, KU Leuven, Leuven, Belgium. ¹⁰Harvard-MIT Division of Health Sciences and Technology, Massachusetts Institute of Technology, Cambridge, MA 02139, USA. ¹¹Massachusetts General Hospital, Boston, MA 02114, USA. ¹²Department of Mechanical Engineering, Massachusetts Institute of Technology, Cambridge, MA 02139, USA.

Received: 3 April 2018 Accepted: 31 October 2018

Published online: 27 November 2018

References

- Gierahn TM, Wadsworth MH, Hughes TK, Bryson BD, Butler A, Satija R, Fortune S, Love JC, Shalek AK. Seq-Well: portable, low-cost RNA sequencing of single cells at high throughput. *Nat Methods*. 2017;14:395.
- Macosko EZ, Basu A, Satija R, Nemesh J, Shekhar K, Goldman M, Tirosh I, Bialas AR, Kamitaki N, Martersteck EM, et al. Highly parallel genome-wide expression profiling of individual cells using nanoliter droplets. *Cell*. 2015;161:1202–14.
- Klein AM, Mazutis L, Akartuna I, Tallapragada N, Veres A, Li V, Peshkin L, Weitz DA, Kirschner MW. Droplet barcoding for single-cell transcriptomics applied to embryonic stem cells. *Cell*. 2015;161:1187–201.
- Easwaran H, Tsai HC, Baylin SB. Cancer epigenetics: tumor heterogeneity, plasticity of stem-like states, and drug resistance. *Mol Cell*. 2014;54:716–27.
- Maier T, Guell M, Serrano L. Correlation of mRNA and protein in complex biological samples. *FEBS Lett*. 2009;583:3966–73.
- Genshaft AS, Li S, Gallant CJ, Darmanis S, Prakadan SM, Ziegler CGK, Lundberg M, Fredriksson S, Hong J, Regev A, et al. Multiplexed, targeted profiling of single-cell proteomes and transcriptomes in a single reaction. *Genome Biol*. 2016;17:15.
- Dey SS, Kester L, Spanjaard B, Bienko M, van Oudenaarden A. Integrated genome and transcriptome sequencing 2015 of the same cell. *Nat Biotechnol*. 33:285.
- Angermueller C, Clark SJ, Lee HJ, Macaulay IC, Teng MJ, Hu TX, Krueger F, Smallwood SA, Ponting CP, Voet T, et al. Parallel single-cell sequencing links transcriptional and epigenetic heterogeneity. *Nat Methods*. 2016;13:229.
- Stoeckius M, Hafemeister C, Stephenson W, Houck-Loomis B, Chattopadhyay PK, Swerdlow H, Satija R, Smibert P. Simultaneous epitope and transcriptome measurement in single cells. *Nat Meth*. 2017; advance online publication.
- Satija R, Farrell JA, Gennert D, Schier AF, Regev A. Spatial reconstruction of single-cell gene expression data. *Nat Biotechnol*. 2015;33:495–U206.
- Achim K, Pettit JB, Saraiva LR, Gavriouchkina D, Larsson T, Arendt D, Marioni JC. High-throughput spatial mapping of single-cell RNA-seq data to tissue of origin. *Nat Biotechnol*. 2015;33:503–U215.
- Stahl PL, Salmen F, Vickovic S, Lundmark A, Navarro JF, Magnusson J, Giacometto S, Asp M, Westholm JO, Huss M, et al. Visualization and analysis of gene expression in tissue sections by spatial transcriptomics. *Science*. 2016;353:78–82.
- Cadwell CR, Palasantza A, Jiang XL, Berens P, Deng QL, Yilmaz M, Reimer J, Shen S, Bethge M, Tolia KF, et al. Electrophysiological, transcriptomic and morphological profiling of single neurons using Patch-seq. *Nat Biotechnol*. 2016;34:199.
- Godin M, Delgado FF, Son SM, Grover WH, Bryan AK, Tzur A, Jorgensen P, Payer K, Grossman AD, Kirschner MW, Manalis SR. Using buoyant mass to measure the growth of single cells. *Nat Methods*. 2010;7:387–U370.
- Son S, Tzur A, Weng Y, Jorgensen P, Kim J, Kirschner MW, Manalis SR. Direct observation of mammalian cell growth and size regulation. *Nat Methods*. 2012;9:910.
- Son S, Stevens MM, Chao HX, Thoreen C, Hosios AM, Schweitzer LD, Weng YC, Wood K, Sabatini D, Vander Heiden MG, Manalis S. Cooperative nutrient accumulation sustains growth of mammalian cells. *Sci Rep*. 2015;5:8.
- Cermak N, Olcum S, Delgado FF, Wasserman SC, Payer KR, A Murakami M, Knudsen SM, Kimmerling RJ, Stevens MM, Kikuchi Y, et al. High-throughput measurement of single-cell growth rates using serial microfluidic mass sensor arrays. *Nat Biotech*. 2016;34:1052–9.
- Stevens MM, Maire CL, Chou N, Murakami MA, Knoff DS, Kikuchi Y, Kimmerling RJ, Liu H, Haidar S, Calistri NL, et al. Drug sensitivity of single cancer cells is predicted by changes in mass accumulation rate. *Nat Biotech*. 2016; advance online publication.
- Calistri NL, Kimmerling RJ, Malinowski S, Stevens MM, Olcum S, Ligon KL, Manalis SR. Microfluidic active loading of single cells enables analysis of complex clinical specimens. *Nat Commun*. 2018.
- Hecht VC, Sullivan LB, Kimmerling RJ, Kim DH, Hosios AM, Stockslager MA, Stevens MM, Kang JH, Wirtz D, Vander Heiden MG, Manalis SR. Biophysical changes reduce energetic demand in growth factor-deprived lymphocytes. *J Cell Biol*. 2016;212:439–47.
- Subramanian A, Tamayo P, Mootha VK, Mukherjee S, Ebert BL, Gillette MA, Paulovich A, Pomeroy SL, Golub TR, Lander ES, Mesirov JP. Gene set enrichment analysis: a knowledge-based approach for interpreting genome-wide expression profiles. *Proc Natl Acad Sci U S A*. 2005;102:15545–50.
- Prakadan SM, Shalek AK, Weitz DA. Scaling by shrinking: empowering single-cell 'omics' with microfluidic devices. *Nat Rev Genet*. 2017;18:17.
- Buettner F, Natarajan KN, Casale FP, Proserpio V, Scialdone A, Theis FJ, Teichmann SA, Marioni JC, Stegic O. Computational analysis of cell-to-cell heterogeneity in single-cell RNA-sequencing data reveals hidden subpopulations of cells. *Nat Biotechnol*. 2015;33:155–60.
- Kowalczyk MS, Tirosh I, Heck D, Rao TN, Dixit A, Haas BJ, Schneider RK, Wagers AJ, Ebert BL, Regev A. Single-cell RNA-seq reveals changes in cell cycle and differentiation programs upon aging of hematopoietic stem cells. *Genome Res*. 2015;25:1860–72.
- Kimmerling RJ, Szeto GL, Li JW, Genshaft AS, Kazer SW, Payer KR, Borrajo JD, Blainey PC, Irvine DJ, Shalek AK, Manalis SR. A microfluidic platform enabling single-cell RNA-seq of multigenerational lineages. *Nat Commun*. 2016;7:7.
- Cetin AE, Stevens MM, Calistri NL, Fulciniti M, Olcum S, Kimmerling RJ, Munshi NC, Manalis SR. Determining therapeutic susceptibility in multiple myeloma by single-cell mass accumulation. *Nat Commun*. 2017;8:1613.

27. Ashburner M, Ball CA, Blake JA, Botstein D, Butler H, Cherry JM, Davis AP, Dolinski K, Dwight SS, Eppig JT, et al. Gene ontology: tool for the unification of biology. *Nat Genet.* 2000;25:25–9.
28. Best JA, Blair DA, Knell J, Yang E, Mayya V, Doedens A, Dustin ML, Goldrath AW, Immunological Genome P. Transcriptional insights into the CD8(+) T cell response to infection and memory T cell formation. *Nat Immunol.* 2013;14:404–12.
29. Fox CJ, Hammerman PS, Thompson CB. Fuel feeds function: energy metabolism and the T-cell response. *Nat Rev Immunol.* 2005;5:844–52.
30. Verbist KC, Guy CS, Milasta S, Liedmann S, Kaminski MM, Wang RN, Green DR. Metabolic maintenance of cell asymmetry following division in activated T lymphocytes. *Nature.* 2016;532:389.
31. Wang RN, Green DR. Metabolic checkpoints in activated T cells. *Nat Immunol.* 2012;13:907–15.
32. Araki K, Morita M, Bederman AG, Konieczny BT, Kissick HT, Sonenberg N, Ahmed R. Translation is actively regulated during the differentiation of CD8(+) effector T cells. *Nat Immunol.* 2017;18:1046.
33. Obst R. The timing of T cell priming and cycling. *Front Immunol.* 2015;6:10.
34. Battle E, Clevers H. Cancer stem cells revisited. *Nat Med.* 2017;23:1124–34.
35. Patel AP, Tirosh I, Trombetta JJ, Shalek AK, Gillespie SM, Wakimoto H, Cahill DP, Nahed BV, Curry WT, Martuza RL, et al. Single-cell RNA-seq highlights intratumoral heterogeneity in primary glioblastoma. *Science.* 2014;344:1396–401.
36. Tirosh I, Izar B, Prakadan SM, Wadsworth MH, Treacy D, Trombetta JJ, Rotem A, Rodman C, Lian C, Murphy G, et al. Dissecting the multicellular ecosystem of metastatic melanoma by single-cell RNA-seq. *Science.* 2016;352:189–96.
37. Barretina J, Caponigro G, Stransky N, Venkatesan K, Margolin AA, Kim S, Wilson CJ, Lehar J, Kryukov GV, Sonkin D, et al. The Cancer Cell Line Encyclopedia enables predictive modelling of anticancer drug sensitivity. *Nature.* 2012;483:603–7.
38. Suva ML, Rheinbay E, Gillespie SM, Patel AP, Wakimoto H, Rabkin SD, Riggi N, Chi AS, Cahill DP, Nahed BV, et al. Reconstructing and reprogramming the tumor-propagating potential of glioblastoma stem-like cells. *Cell.* 2014;157:580–94.
39. Chene P. Inhibiting the p53-MDM2 interaction: an important target for cancer therapy. *Nat Rev Cancer.* 2003;3:102–9.
40. Verreault M, Schmitt C, Goldwirt L, Pelton K, Haidar S, Levasseur C, Guehenec J, Knoff D, Labussiere M, Marie Y, et al. Preclinical efficacy of the MDM2 inhibitor RG7112 in MDM2-amplified and TP53 wild-type glioblastomas. *Clin Cancer Res.* 2016;22:1185–96.
41. Fischer M. Census and evaluation of p53 target genes. *Oncogene.* 2017;36:3943–56.
42. Saxton RA, Sabatini DM. mTOR signaling in growth, metabolism, and disease. *Cell.* 2017;168:960–76.
43. Song MS, Salmena L, Pandolfi PP. The functions and regulation of the PTEN tumour suppressor. *Nat Rev Mol Cell Biol.* 2012;13:283–96.
44. Wee KB, Surana U, Aguda BD. Oscillations of the p53-Akt network: implications on cell survival and death. *PLoS One.* 2009;4:13.
45. Daniele S, Costa B, Zappelli E, Da Pozzo E, Sestito S, Nesi G, Campiglia P, Marinelli L, Novellino E, Rapposelli S, Martini C. Combined inhibition of AKT/mTOR and MDM2 enhances Glioblastoma Multiforme cell apoptosis and differentiation of cancer stem cells. *Sci Rep.* 2015;5:14.
46. Buenostro JD, Wu BJ, Litzenburger UM, Ruff D, Gonzales ML, Snyder MP, Chang HY, Greenleaf WJ. Single-cell chromatin accessibility reveals principles of regulatory variation. *Nature.* 2015;523:486–U264.
47. Shalek AK, Benson M. Single-cell analyses to tailor treatments. *Sci Transl Med.* 2017;9:3.
48. Trombetta JJ, Gennert D, Lu D, Satija R, Shalek AK, Regev A. Preparation of single-cell RNA-Seq libraries for next generation sequencing. *Curr Protoc Mol.* 2014;107:4.22.21–24.22.17.
49. Picelli S, Bjorklund AK, Faridani OR, Sagasser S, Winberg G, Sandberg R. Smart-seq2 for sensitive full-length transcriptome profiling in single cells. *Nat Methods.* 2013;10:1096–8.
50. Li B, Dewey CN. RSEM: accurate transcript quantification from RNA-Seq data with or without a reference genome. *Bmc Bioinformatics.* 2011;12:16.
51. Kim D, Pertea G, Trapnell C, Pimentel H, Kelley R, Salzberg SL. TopHat2: accurate alignment of transcriptomes in the presence of insertions, deletions and gene fusions. *Genome Biol.* 2013;14:13.
52. Sergushichev A. An algorithm for fast preranked gene set enrichment analysis using cumulative statistic calculation. *bioRxiv.* 2016. <https://doi.org/10.1101/060012>.
53. Kimmerling RJ, Prakadan SM, Gupta AJ, Calistri NL, Stevens MM, Olcum S, Cermak N, Drake RS, Pelton K, De Smet F, Ligon KL, Shalek AK, Manalis SR. Linking single-cell measurements of mass, growth rate, and gene expression. *Gene Expression Omnibus.* 2018. <https://www.ncbi.nlm.nih.gov/geo/query/acc.cgi?acc=GSE121655>.
54. Kimmerling RJ, Prakadan SM, Gupta AJ, Calistri NL, Stevens MM, Olcum S, Cermak N, Drake RS, Pelton K, De Smet F, Ligon KL, Shalek AK, Manalis SR. Linking single-cell measurements of mass, growth rate, and gene expression. *GitHub repository.* <https://github.com/rjkimmer/linkedMeasurementAnalysis>. 2018.

Ready to submit your research? Choose BMC and benefit from:

- fast, convenient online submission
- thorough peer review by experienced researchers in your field
- rapid publication on acceptance
- support for research data, including large and complex data types
- gold Open Access which fosters wider collaboration and increased citations
- maximum visibility for your research: over 100M website views per year

At BMC, research is always in progress.

Learn more biomedcentral.com/submissions



Figure S1

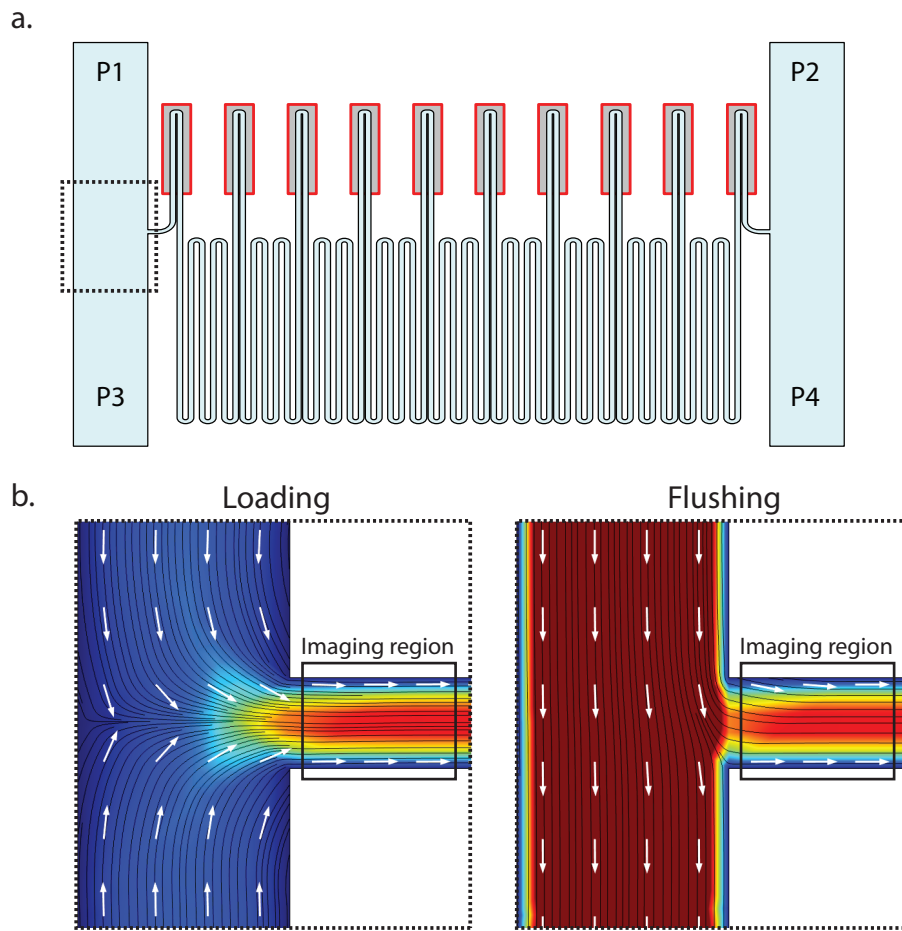


Figure S1 | Fluidic regimes for maintaining cell spacing in the sSMR

(a) Schematic of sSMR presented in **Figure 1** denoting the array entrance region used for fluidic simulation presented in **(b)** (dashed box outline). **(b)** COMSOL fluidic simulations demonstrating the loading (left) and flushing (right) fluidic regimes described in **Additional File 1: Note S1**. The imaging region used to trigger between each fluidic state is outlined (solid box).

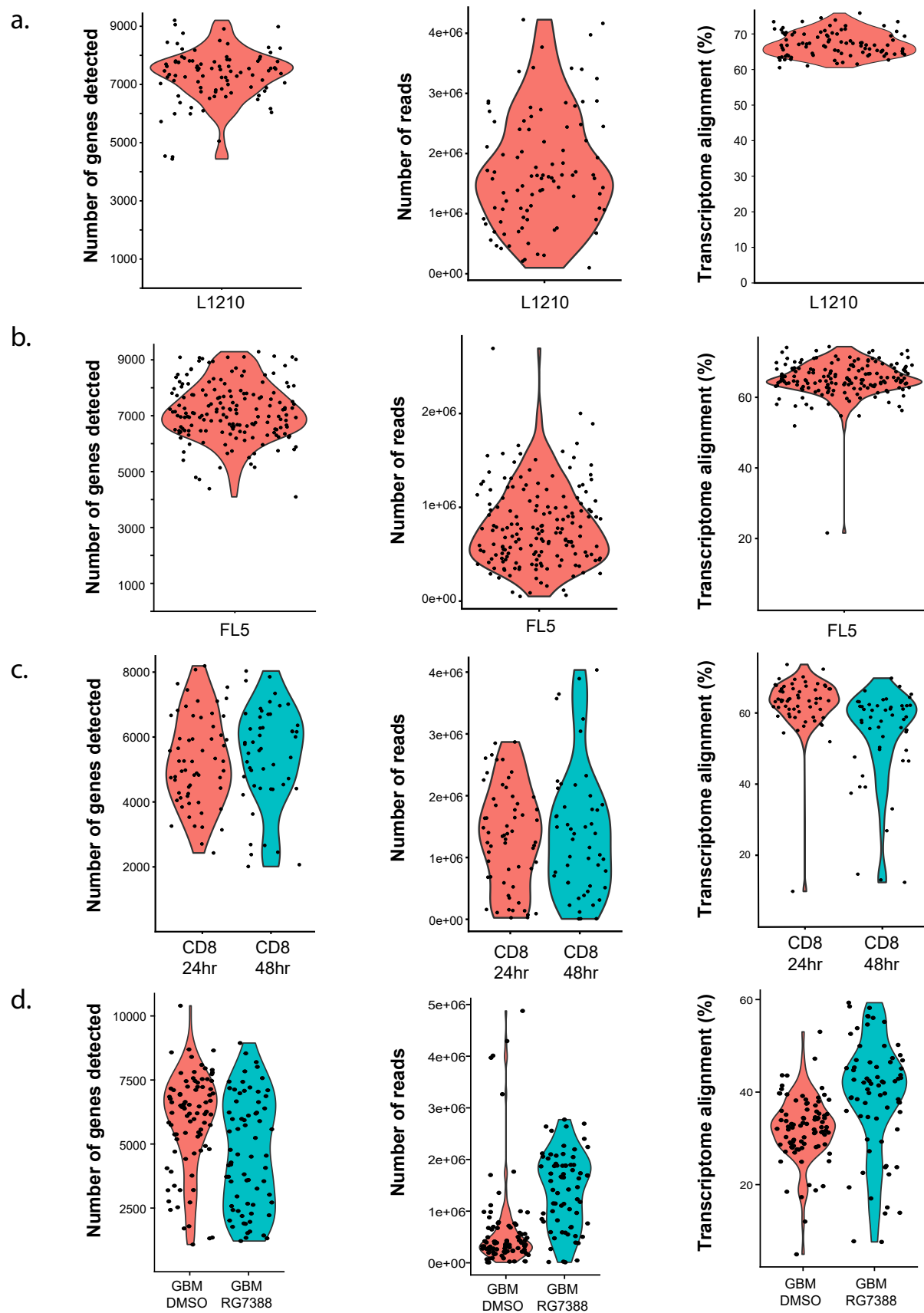


Figure S2 | Quality metrics for scRNA-seq libraries

Violin plots and overlaid points showing the number of genes detected (left), sequencing depth (center), and transcriptome alignment (right) for each scRNA-seq library prepared for **(a)** L1210 cells, **(b)** FL5.12 cells **(c)** CD8+ T cells activated for either 24 or 48h (red and blue outlines, respectively), and **(d)** BT159 GBM cells treated with either DMSO or RG7388 (red and blue outlines, respectively) that passed initial quality thresholds and were used for further analysis (**Methods**).

Figure S3

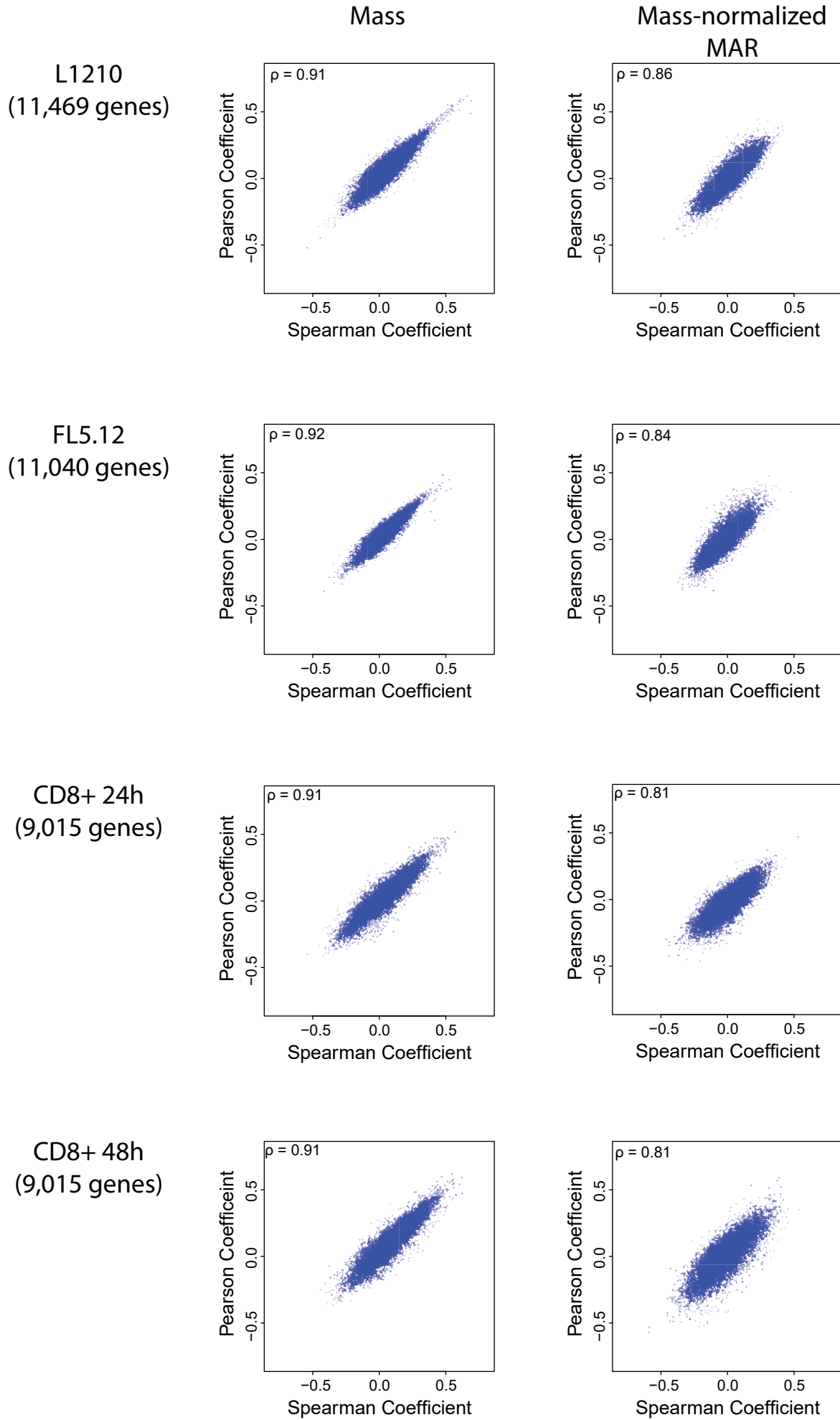


Figure S3 (continued)

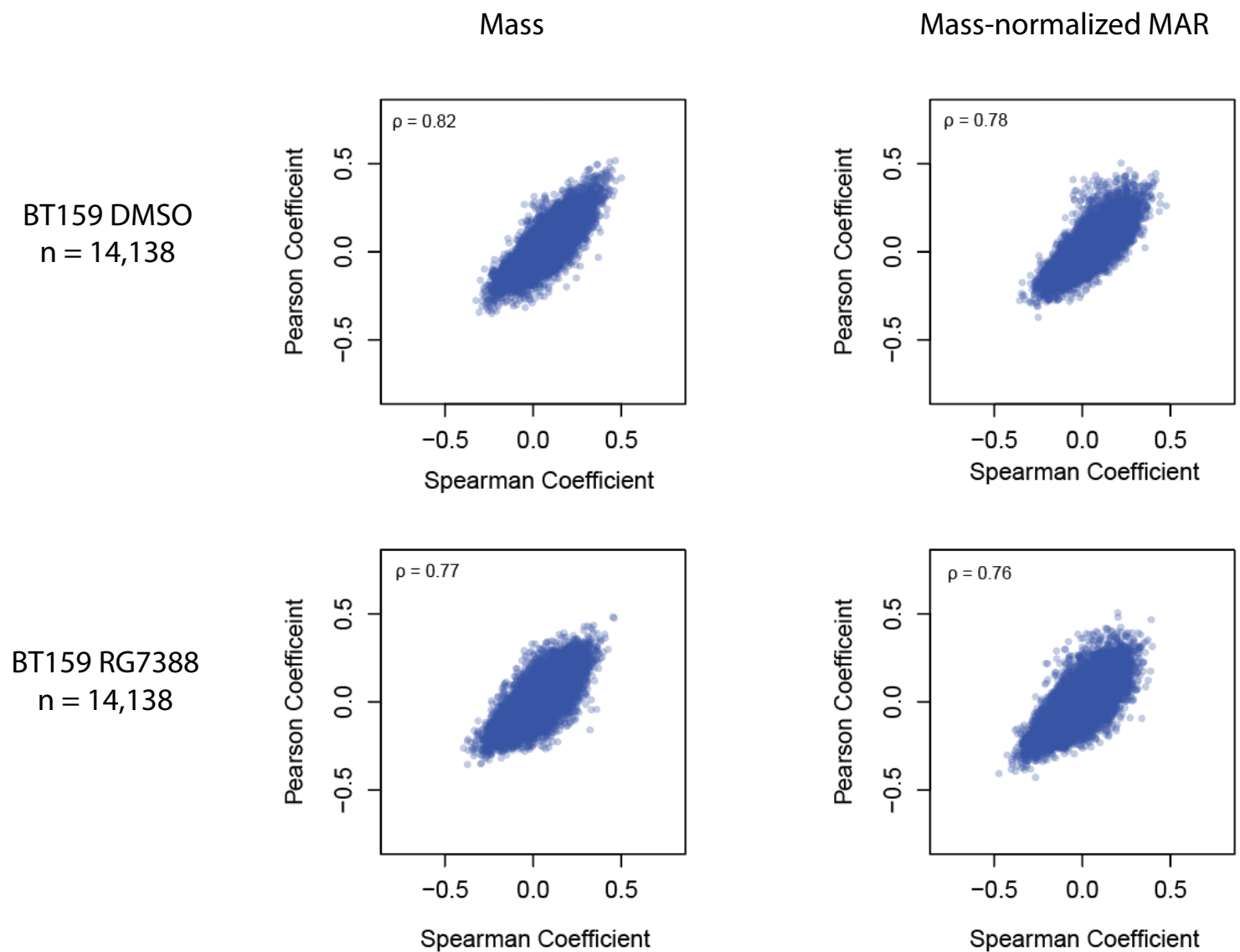
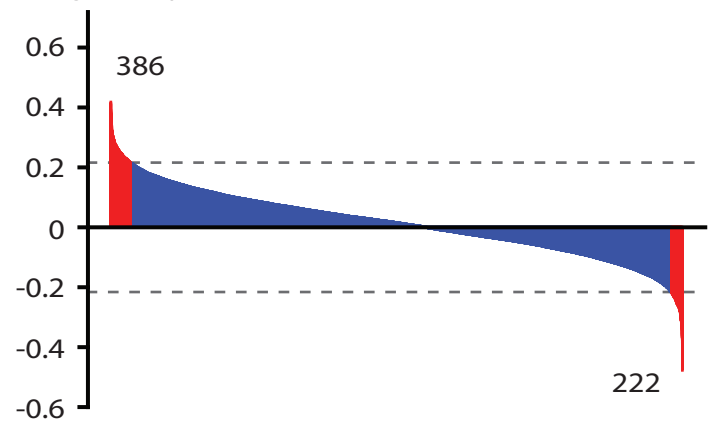
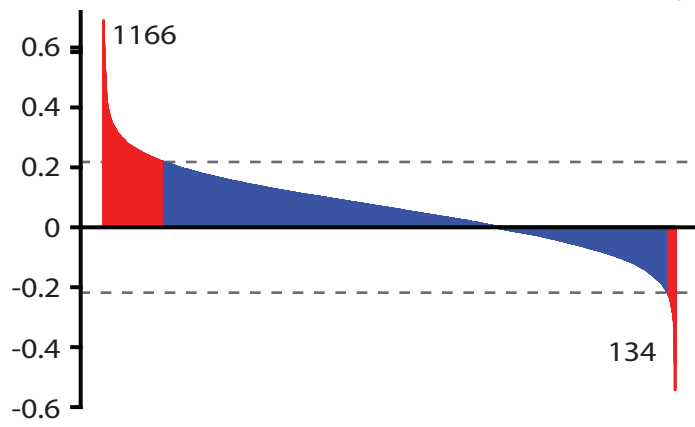


Figure S3 | Comparison of Pearson and Spearman coefficients for correlations between gene expression and biophysical parameters

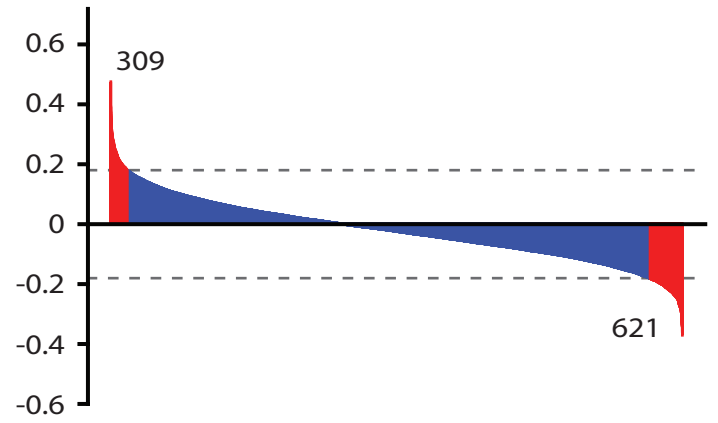
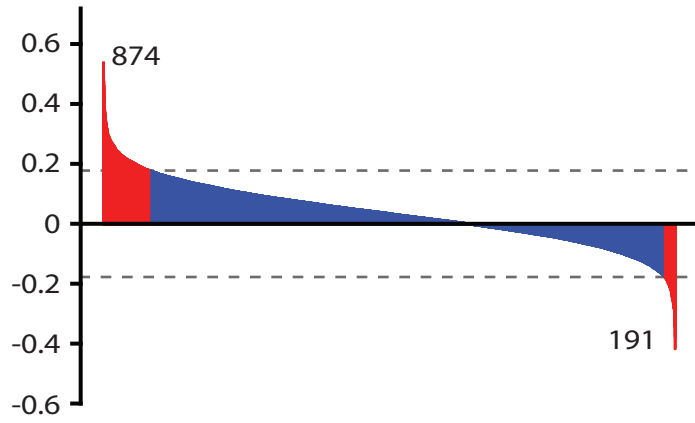
Plots of the Pearson coefficient versus Spearman coefficient for expression level correlations with either mass (left column) or mass-normalized MAR (right column) for L1210, FL5.12, CD8+ T cells (24 and 48h time points), and BT159 GBM cells (DMSO and RG7388 treated). Each cell type lists the total number of genes being compared and each plot indicates the Spearman coefficient between the Spearman and Pearson coefficients across all genes. Each measurement set reveals similar gene-level rankings for both Spearman and Pearson coefficients.

Figure S4

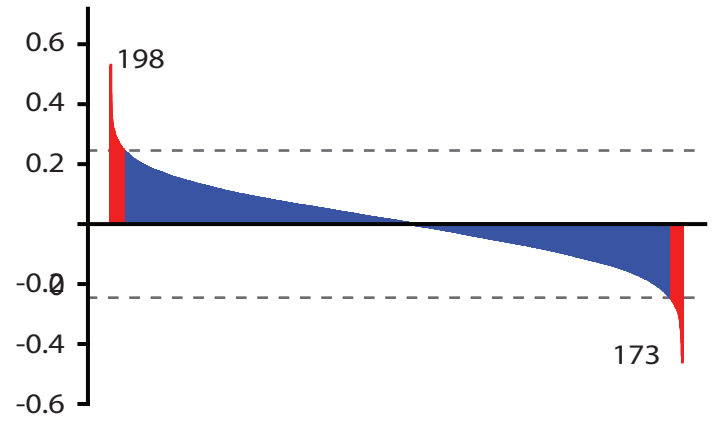
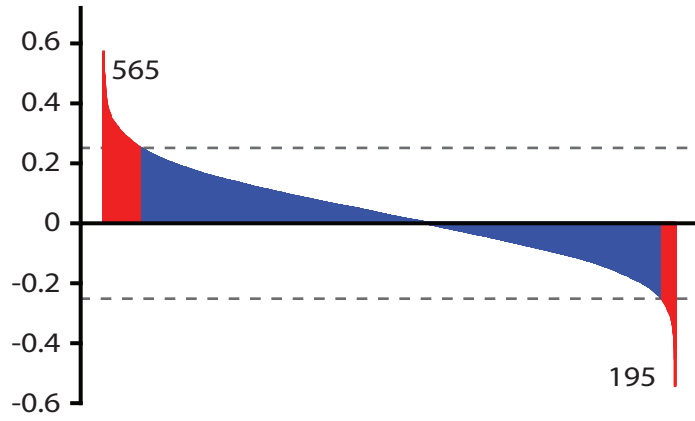
L1210 (11,469 genes)



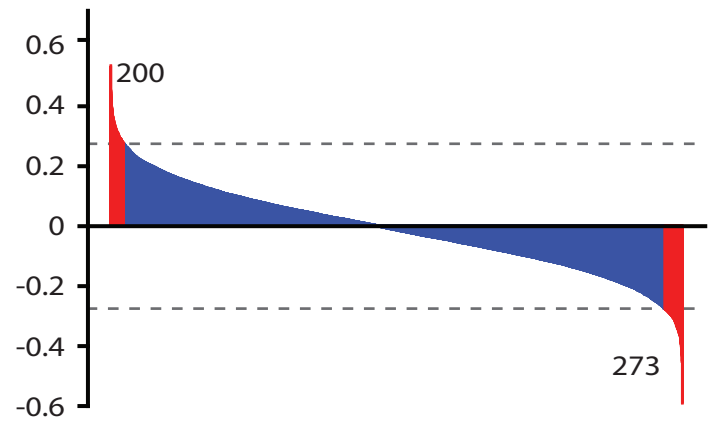
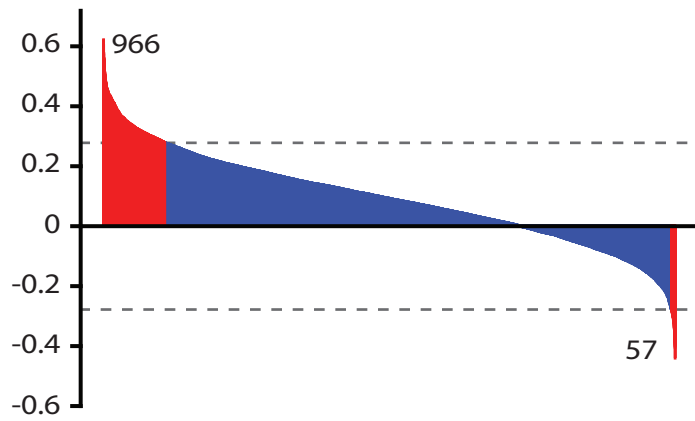
FL5.12 (11,040 genes)



CD8+ 24h (9,015 genes)



CD8+ 48h (9,015 genes)



Spearman coefficient (ρ)

Genes ranked by Spearman coefficient

Figure S4 (continued)

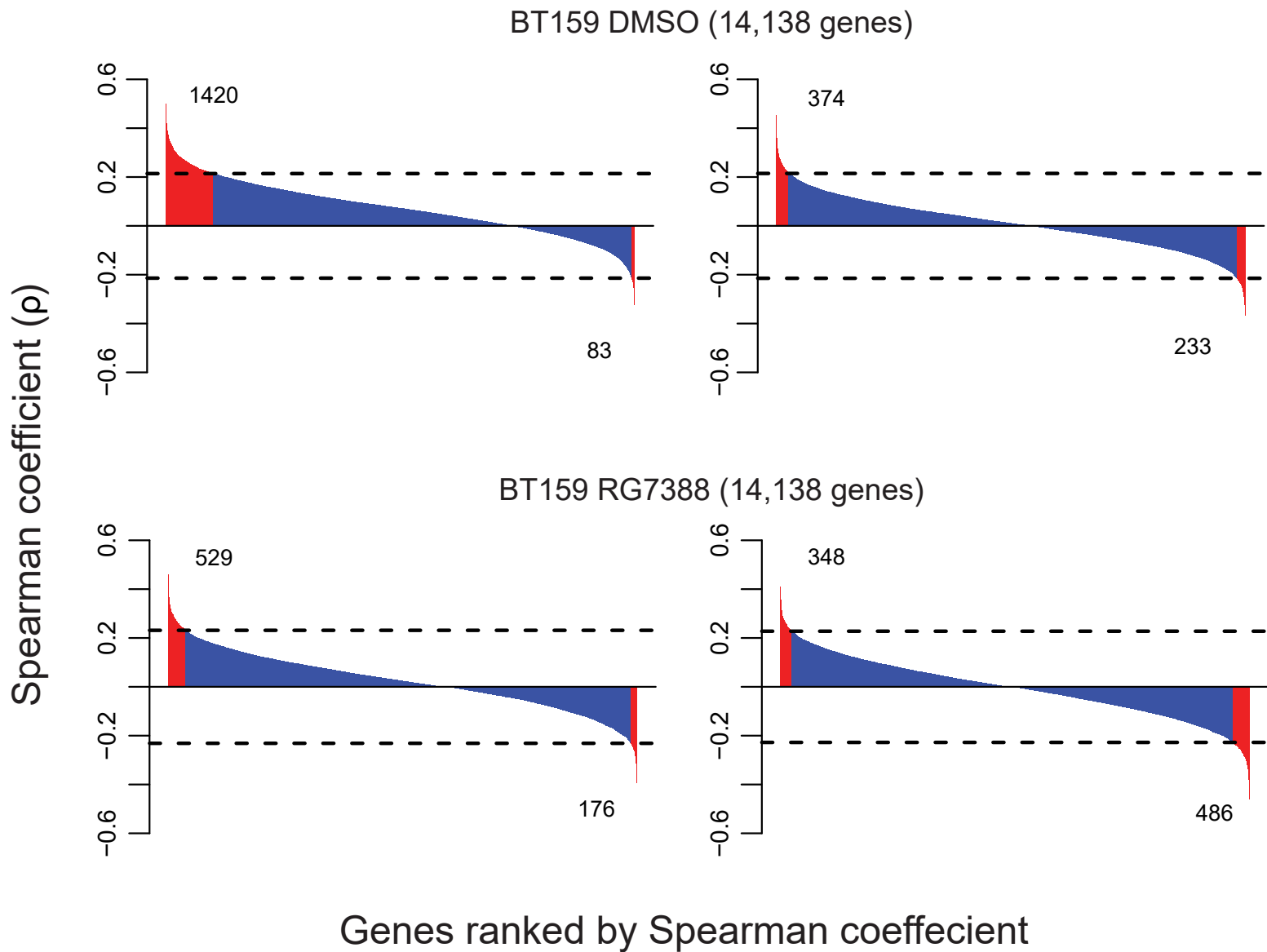
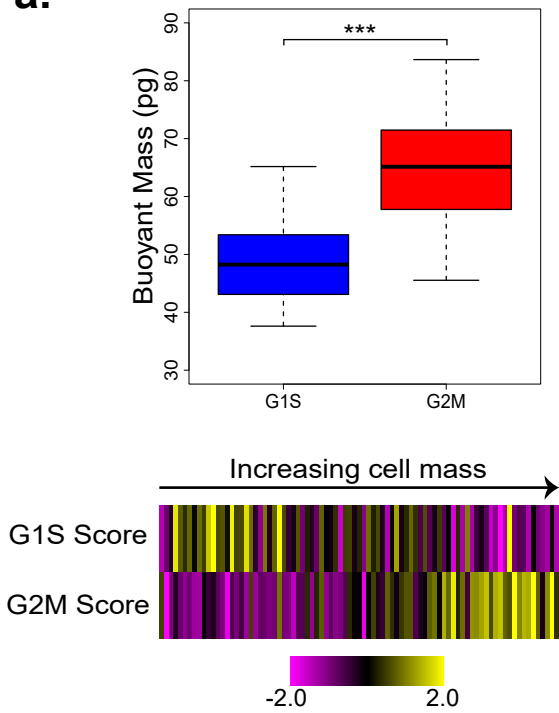


Figure S4 | Expression level correlation with biophysical parameters for L1210, FL5.12, CD8+ T cells, and BT159 GBM cells

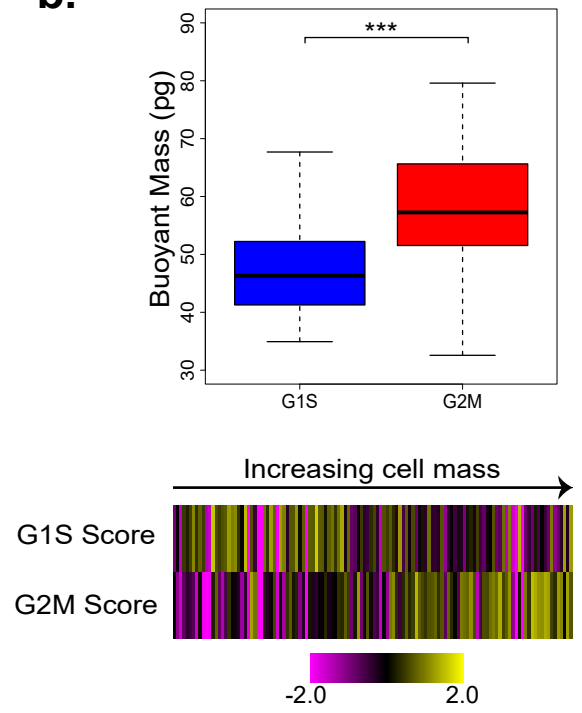
Bar plots denoting the correlation strength of individual gene's expression levels with either mass (left) or mass-normalized MAR (right) for (a) L1210 cells ($n = 11,469$ genes), (b) FL5.12 cells ($n = 11,040$ genes), (c) CD8+ T cells after 24h of activation ($n = 9,015$ genes), (d) CD8+ T cells after 48h of activations ($n = 9,015$ genes), (e) BT159 cells treated with DMSO ($n = 14,138$ genes), and (f) BT159 cells treated with RG7388 ($n = 14,138$ genes). Genes are plotted in rank order where genes with highest positive and negative correlations with biophysical parameters are found at the left-most and right-most portion of the x axis, respectively. For each data set, a null distribution of correlation coefficients was determined by finding the correlation between gene expression and mass for randomly permuted data. After 10 iterations, we determined the average standard deviation of these distributions of correlation coefficients. Any individual gene that had a correlation coefficient with an absolute value greater than twice the standard deviation ($P < 0.05$, denoted by the dashed lines in the plots) was considered significant (red bars), all genes presented as blue bars fell below this threshold. The number of genes showing a significant positive or negative correlation with the biophysical parameter of interest are shown in each plot.

Figure S5

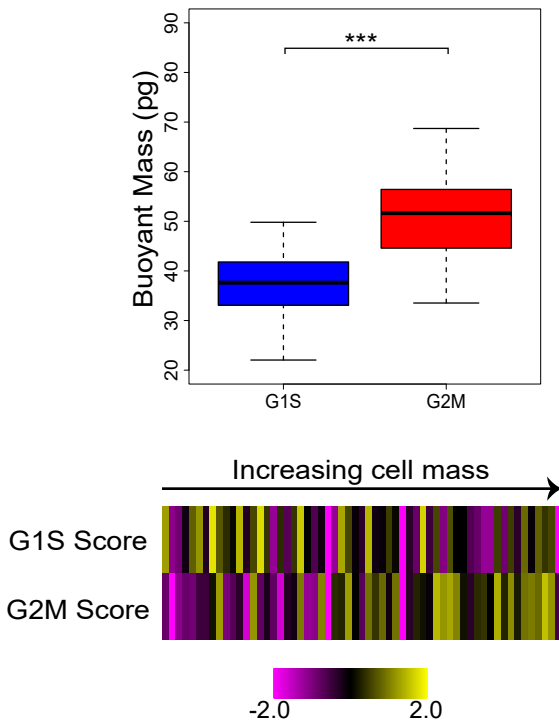
a.



b.



c.



d.

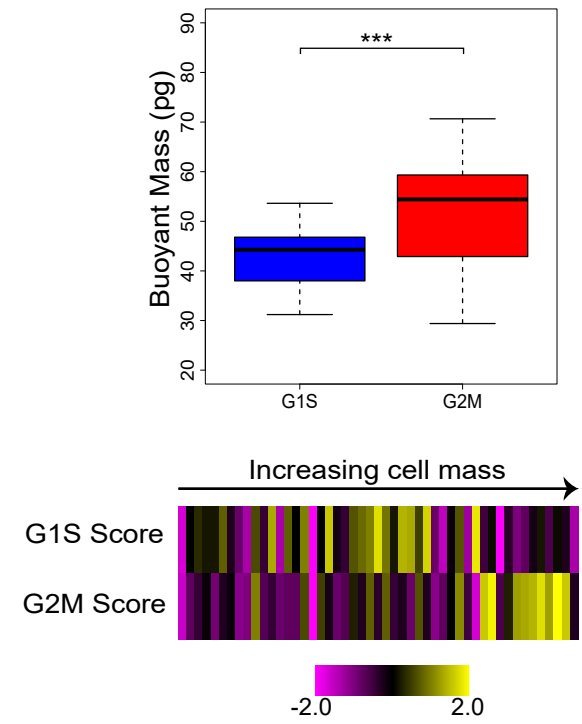


Figure S5 | Comparison of cell cycle gene expression and cell mass

Boxplots (top) showing the mass distribution of single-cells classified as being in the G1/S or G2/M phases of the cell cycle as described in **Additional File 1: Note S3** for **(a)** L1210 cells ($n = 48$ and 37 for G1/S and G2/M, respectively), **(b)** FL5.12 ($n = 63$ and 61 for G1/S and G2/M, respectively), **(c)** CD8⁺ T cells after 24h of activation ($n = 25$ and 34 for G1/S and G2/M, respectively), and **(d)** CD8⁺ T cells after 48h of activation ($n = 25$ and 24 for G1/S and G2/M, respectively) (***) indicates $P < 0.001$, Mann-Whitney U Test). Below each boxplot is a heatmap showing the G1/S and G2/M expression scores for cells ranked by buoyant mass, also as described in **Additional File 1: Note S3**.

Figure S6

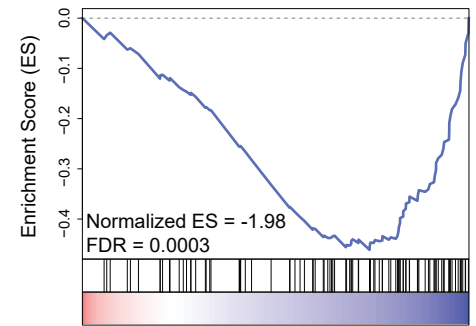
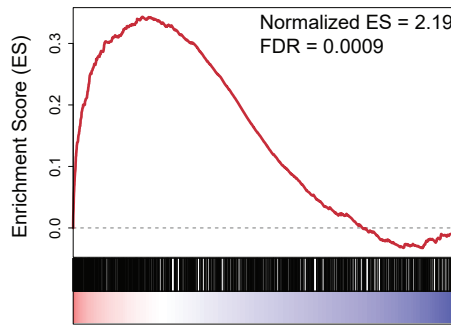
a.

— L1210 genes with significant positive correlation with mass (n = 1,166, left panel)

— L1210 genes with significant negative correlation with mass (n = 134, right panel)

Positive Negative

L1210 genes ranked by correlation with single-cell time since division (n = 11,142) [25]



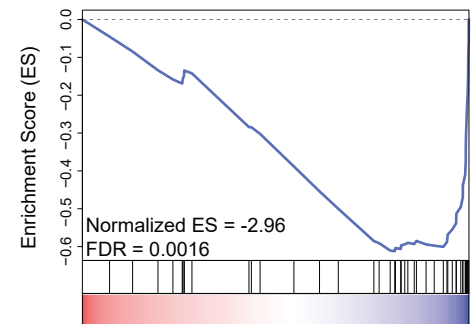
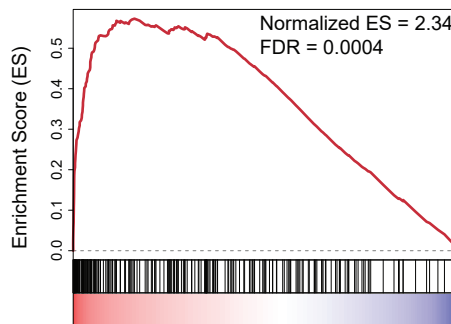
b.

— FL5.12 genes with significant positive correlation with mass (n = 874, left panel)

— FL5.12 genes with significant negative correlation with mass (n = 191, right panel)

Positive Negative

FL5.12 genes ranked by correlation with single-cell mass in a second replicate experiment (n = 10,323)



c.

— FL5.12 genes with significant positive correlation with mass-normalized MAR (n = 309, left panel)

— FL5.12 genes with significant negative correlation with mass-normalized MAR (n = 621, right panel)

Positive Negative

FL5.12 genes ranked by correlation with single-cell mass-normalized MAR in a second replicate experiment (n = 10,323)

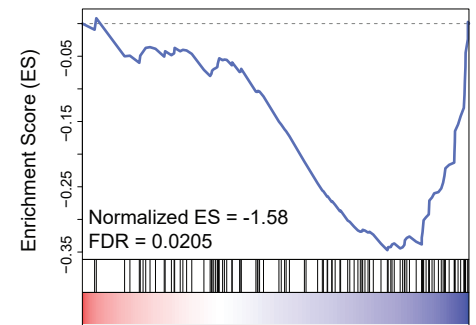
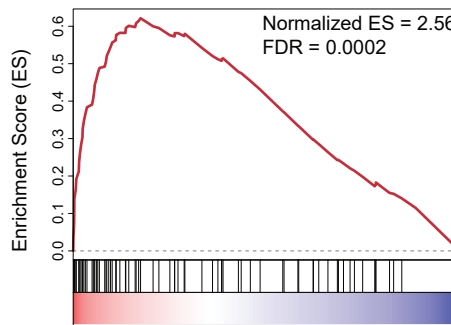


Figure S6 | Reproducibility of linked measurements for L1210 and FL5.12 cells

(a) Enrichment plots for genes with significant positive (left, n = 1,166) or negative (right, n = 134) correlations with single-cell mass amongst genes ranked by expression level correlation with time since division in L1210 cells – determined by Kimmerling et al. (**Additional File 1: Note S2**) [25]. Significant enrichment (FDR = 0.0009 and 0.0003 for positive and negative sets, respectively) suggests that a consistent cell cycle gene expression signature correlates with both cell mass and time since division in L1210 cells. **(b)** Enrichment plots for genes with significant positive (left, n = 874) and negative (right, n = 191) correlations with FL5.12 cell mass amongst a full gene list ranked by expression level correlation with FL5.12 cell mass from a second, independent experiment. The significant enrichment here (FDR = 0.0004 and 0.0016 for positive and negative sets, respectively) demonstrates a reproducible gene expression signature corresponding to FL5.12 mass. **(c)** Same analysis as in **(b)** for genes that correlated significantly with mass-normalized growth rate (growth efficiency, n = 309 and 621 genes for positive and negative correlations, respectively) as opposed to mass, demonstrating reproducible growth-related gene expression signatures as well (FDR = 0.0002 and 0.0205 for positive and negative sets, respectively).

Figure S7

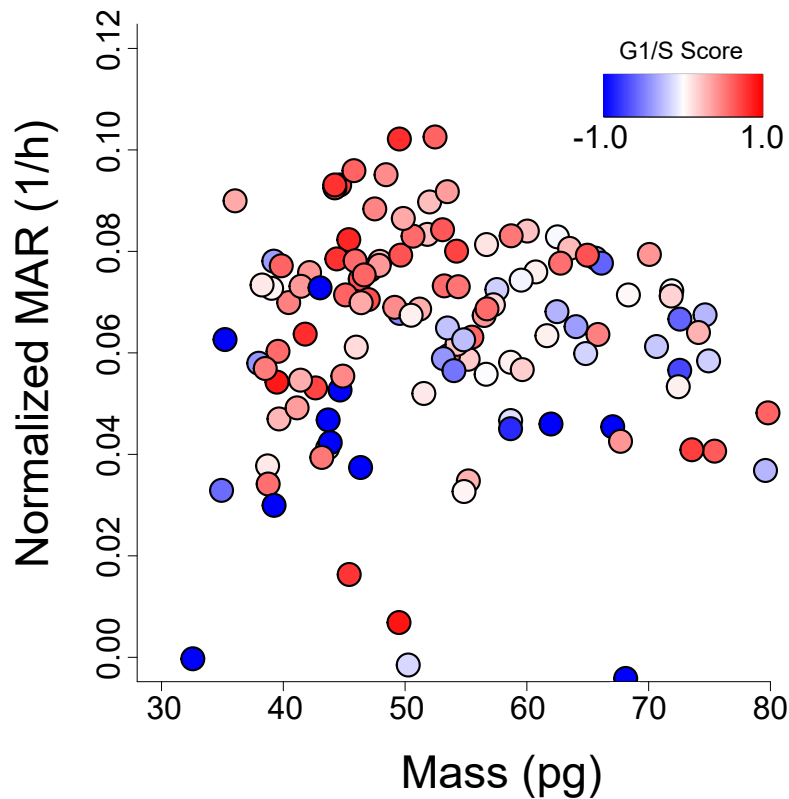


Figure S7 | Cell cycle gene expression versus normalized growth rate in FL5.12 cells

Plot of mass versus mass-normalized growth rate (growth efficiency) for a subset of the FL5.12 cells depicted in **Figure 2** that were captured downstream for scRNA-seq ($n = 124$). Points are colored by G1/S score. The “cell cycle G1/S phase transition” gene ontology term was found to be significantly enriched amongst genes ranked by correlation with growth efficiency. To determine the G1/S transition scores for single FL5.12 cells, we found the average of mean-centered, z-score scaled expression values for the genes in the “cell cycle G1/S phase transition” gene ontology term found to correlate significantly with normalized growth rate ($n = 13$ genes, **Additional File 1: Figure S4, Additional File 5: Table S4**) [21].

Figure S8

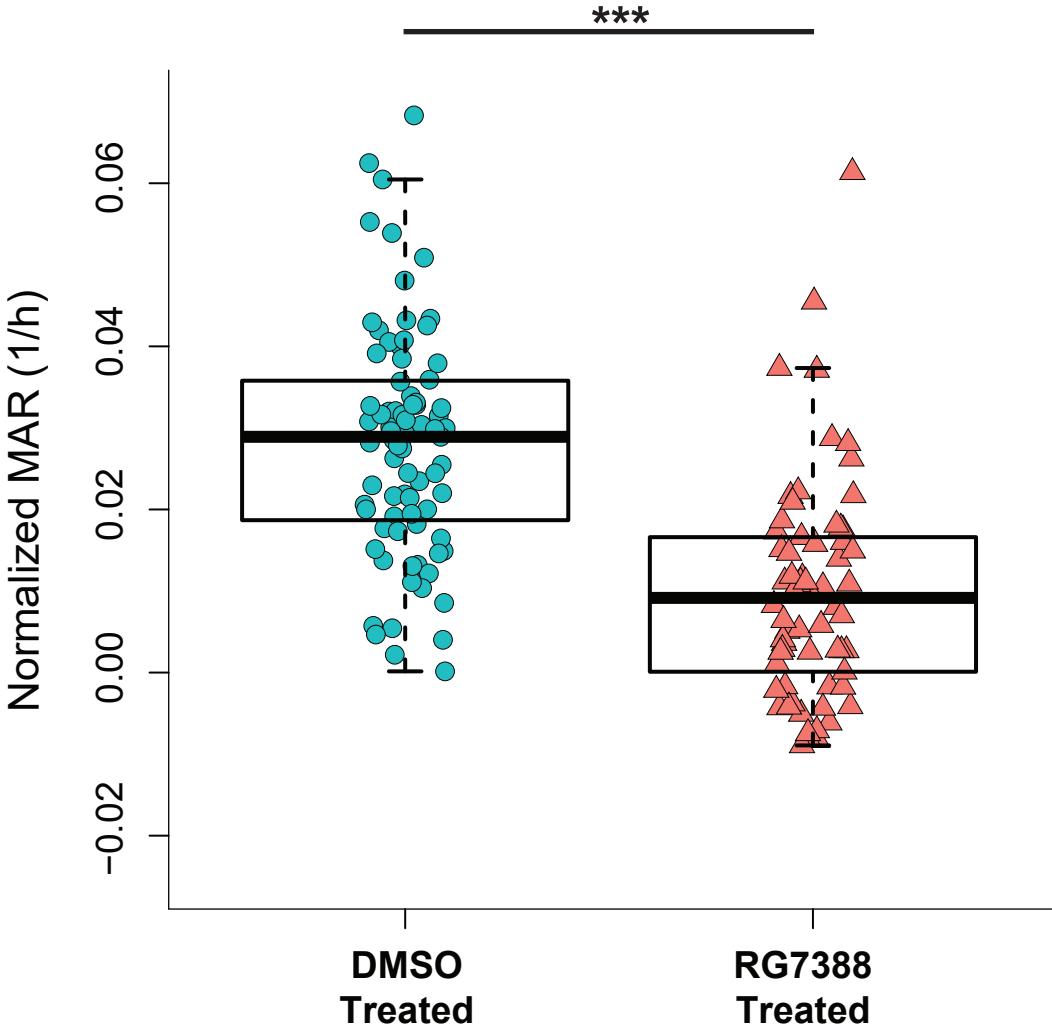


Figure S8 | Mass-normalized MAR measurements for BT159 cells

Single-cell mass-normalized MAR measurements and corresponding boxplots for BT159 cells treated for 16h with either DMSO (left, n = 83) or RG7388 (right, n = 66). *** indicates P < 0.001, Mann-Whitney U-test.

Figure S9

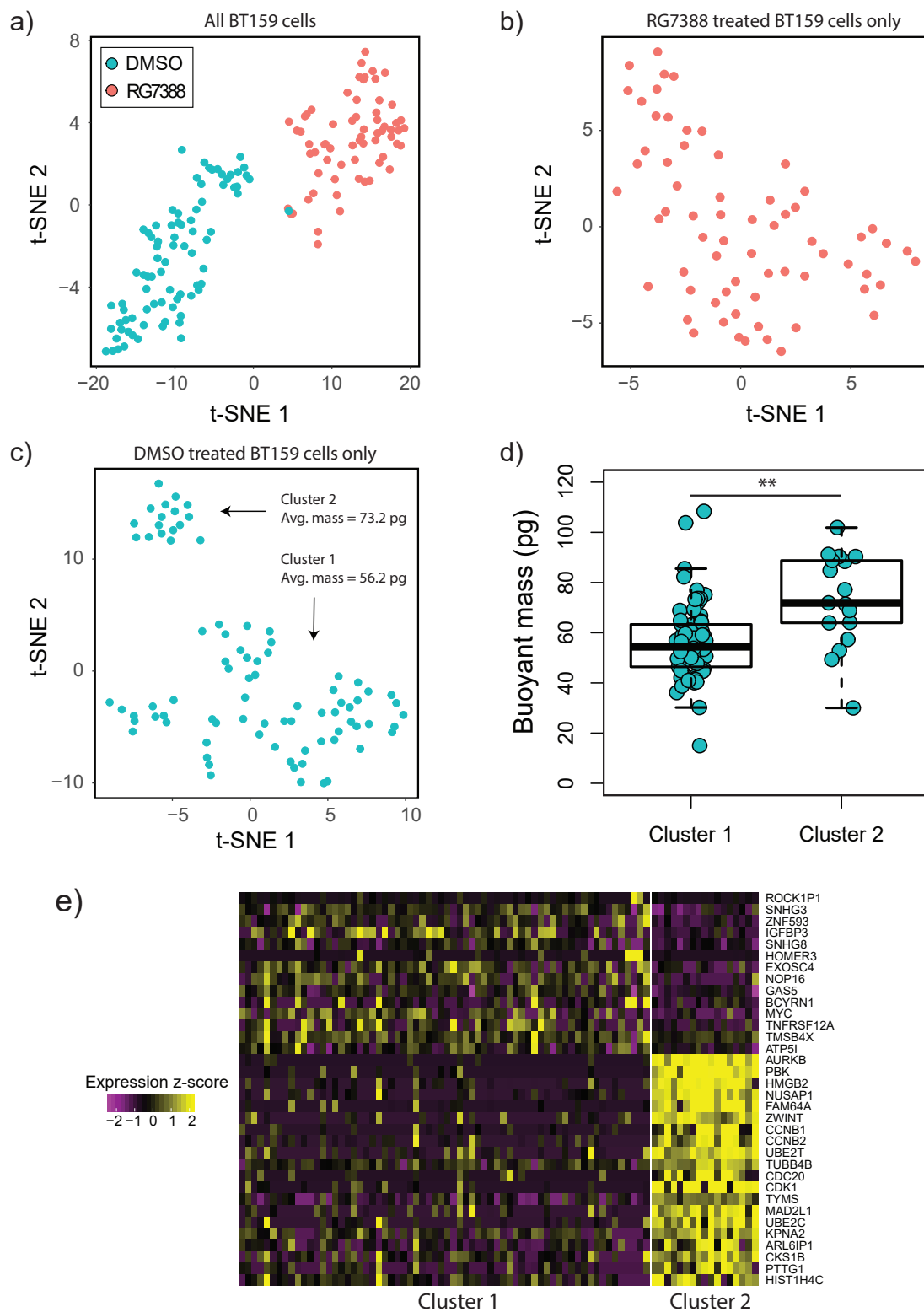


Figure S9 | *t*-SNE analysis of BT159 cells

(a) *t*-SNE plot of both DMSO treated ($n = 83$, blue points) and RG7388 treated ($n = 66$, red points) BT159 cells analyzed together. **(b)** *t*-SNE plot of RG7388 treated BT159 cells alone. **(c)** *t*-SNE plot of DMSO treated BT159 cells alone. Annotations indicate the two distinct subpopulations identified by KNN clustering over significant PCs and the corresponding average masses of cells within these clusters. **(d)** Single-cell mass measurements and corresponding boxplots for two clusters ($n = 66$ and $n = 17$ for Cluster 1 and Cluster 2, respectively) of DMSO treated BT159 cells identified in **(c)**. ** Indicates $P < 0.01$, Mann-Whitney U-test. **(e)** Heatmap showing z-score scaled expression values for genes defining the two clusters depicted in **(c)**. Cluster 2, which is composed of cells with a significantly higher mass ($P < 0.01$, Mann-Whitney U-test), shows increased expression of various genes relating to cell cycle progression.

Figure S10

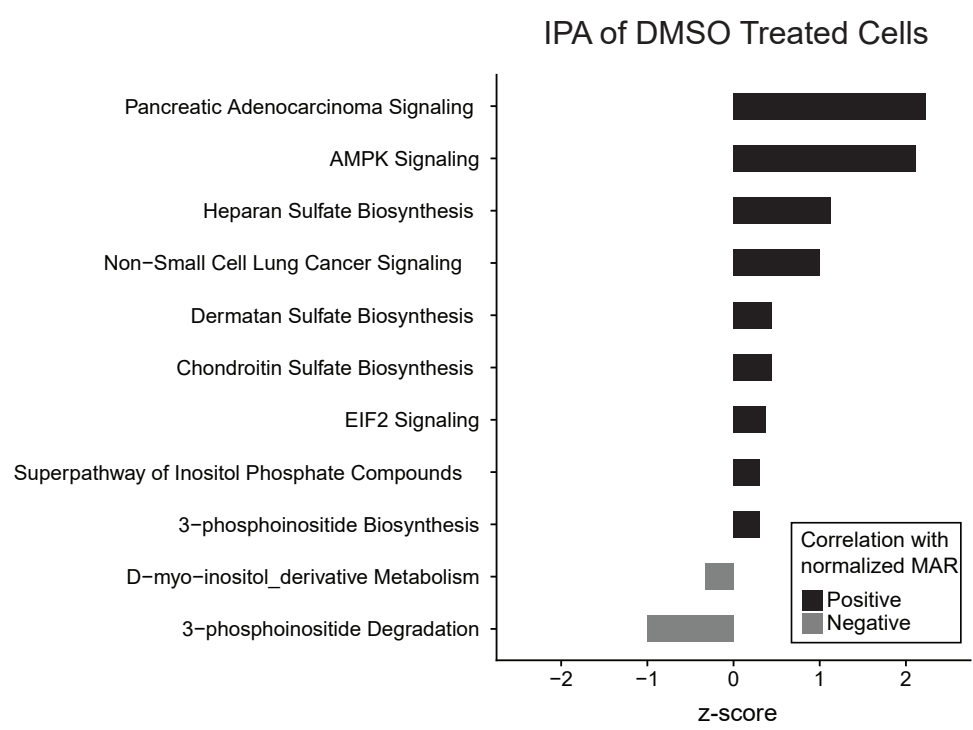


Figure S10 | IPA of DMSO treated BT159 cells

Plot of significantly enriched canonical pathways (FDR<0.05) in DMSO treated BT159 cells (n = 83), as determined by Ingenuity Pathway Analysis, amongst genes with significant positive (black) or negative (gray) correlations with normalized MAR. (**Additional File 1: Figure S4, Additional File 11: Table S10, Methods**).

Supplementary Notes

Note S1 | Maintaining minimum cell spacing in mass sensor array

Loading single cells into the mass sensor array at a fixed, minimum spacing requires the implementation of active switching between two distinct fluidic states. Initially, equivalent pressures are applied to the upstream and downstream ports on the bypass channel leading in to the array (**Additional File 1: Figure S1**, ports P1 and P3). In this “loading” configuration, all streamlines are directed into the array and therefore cells in the bypass channel will enter the array. An imaging region at the entrance to the mass sensor array (outlined in **Additional File 1: Figure S1**) is used as an indication of when a cell has been successfully loaded. Real-time optical peak detection within this region is used to switch from this loading fluidic state to a “flushing” regime wherein the upstream pressures (P1) is increased and the downstream pressure (P3) is decreased such that a vast majority of streamlines continue along the bypass channel with a small fraction entering the array. Because cells are of finite size and occupy several streamlines, they are directed along the bypass channel and not drawn in to the array. Importantly, during this process the pressure at the entrance to the mass sensor array is maintained at a fixed value, therefore any cells that have entered the array continue to flow at a constant speed. Therefore, although the volumetric flow rate is maintained across the array while flushing, no additional cells are loaded. After a desired amount of time has elapsed the system is automatically returned to the loading configuration to obtain the next cell for measurement.

Note S2 | Determining reproducibility of gene signatures related to mass and MAR

In order to determine the reliability and reproducibility of the linked biophysical and gene expression profiles, it was important to compare these signatures with additional results collected from independent experiments. For L1210 cells, single-cell gene expression profiles had previously been collected for cells with known times since division (TSD), a proxy for cell cycle progression [25]. We therefore hypothesized that the list of genes with expression levels that correlated significantly with single-cell mass (an alternative proxy for cell cycle progression) would show significant overlap with genes that correlated strongly with TSD. To determine the extent of this similarity, we constructed two test gene sets for gene set enrichment analyses: one which included genes with a significant positive correlation with cell mass and another which included genes with a significant negative correlation with cell mass (**Additional File 1: Figure S6a, Additional File 2: Table S1**). These gene subsets were compared to the full L1210 gene list measured previously, with genes ranked by how strongly their expression levels correlated with TSD. Genes with a significant positive correlation with mass were significantly over-represented amongst genes that showed a positive correlation with TSD in prior measurements (FDR<0.05). Similarly, genes with a significant negative correlation with mass were significantly over-represented amongst genes that showed a negative correlation with TSD (FDR<0.05). These results indicate that similar sets of genes are correlated with both TSD and single-cell mass, suggesting consistency between the measurements collected here and those collected previously.

Next, we sought to perform a similar comparison for FL5.12 cells. However, in contrast to L1210 cells, no single-cell gene expression measurements had been collected for these cells previously. We therefore conducted a second, independent experiment where single-cell mass and MAR measurements were

collected upstream of scRNA-seq for FL5.12 cells (**Additional File 1: Figure S6b,c**). Using this independent data set, we generated full gene lists that were ranked by correlation strength with either mass or mass-normalized MAR. Then we once again constructed test gene sets, this time containing genes from the original FL5.12 data set with significant correlations (both positive and negative) with either mass or mass-normalized MAR ($P < 0.05$). Following the same analysis described above, we found that gene sets correlating with both mass and mass-normalized MAR showed significant overlap between both replicate experiments ($FDR < 0.05$). This once again demonstrates the reproducibility of the gene expression signatures that correlate with single-cell biophysical properties.

Note S3 | Additional cell cycle gene expression analysis

To further validate the cell cycle-related gene expression signatures that correlated with cell mass, we performed an additional set of analyses relying on single-cell gene expression data alone modelled after the cell cycle interpretation approaches presented by Macosko et al. and Kowalczyk et al. [2, 24]. Briefly, we utilized gene lists found to be associated with the G1/S and G2/M stages of the cell cycle reported by Whitfield et al. [53]. Rough phase-specific scores were determined by calculating the average expression value ($\ln(\text{TPM}+1)$) of genes from these lists that were detected in the data set of interest (L1210, FL5.12, or CD8+ T cells). The lists used for each phase were then filtered to only include genes that correlated strongly ($R > 0.3$) with these rough scores. The average expression values across these remaining genes were then mean centered and divided by their standard deviation to yield the final G1/S and G2/M phase-specific scores. Each individual cell was assigned to either the G1/S or G2/M phases based on which gene list yielded the maximal score. For all cell types, the mass of cells assigned to the G2/M phase were significantly greater than those assigned to the G1/S phase ($P < 0.001$, Mann-Whitney U Test, boxplots in **Additional File 1: Figure S5**). Furthermore, cells ranked by mass showed clear negative and positive relationships with G1/S and G2/M scores, respectively (heatmaps in **Additional File 1: Figure S5**). These results offer further evidence of a coordination between single-cell mass and cell cycle gene expression in L1210, FL5.12, and CD8+ T cells at various stages of activation.